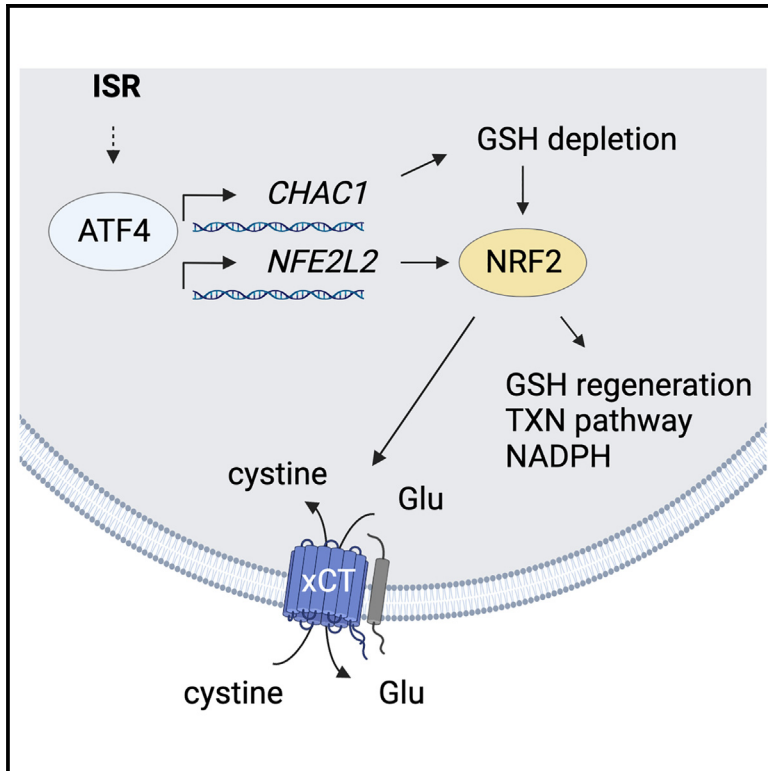


The integrated stress response effector ATF4 is an obligatory metabolic activator of NRF2

Graphical abstract



Authors

Julia Katharina Charlotte Kreß,
Christina Jessen, Anita Hufnagel, ...,
Colin R. Goding,
José Pedro Friedmann Angeli,
Svenja Meierjohann

Correspondence

svenja.meierjohann@uni-wuerzburg.de

In brief

Kreß et al. present a comprehensive explanation of the link between the integrated stress response (ISR) and the transcription factor NRF2. The study highlights how the ISR effector ATF4 augments NRF2 through a combination of transcriptional and metabolic mechanisms, thereby adding an additional layer to the ISR.

Highlights

- The integrated stress response leads to a general ATF4-dependent activation of NRF2
- ATF4 causes a CHAC1-dependent GSH depletion, resulting in NRF2 stabilization
- An elevation of NRF2 transcript levels fosters this effect
- NRF2 supports the ISR/ATF4 pathway by improving cystine and antioxidant supply



Article

The integrated stress response effector ATF4 is an obligatory metabolic activator of NRF2

Julia Katharina Charlotte Kreß,¹ Christina Jessen,¹ Anita Hufnagel,¹ Werner Schmitz,² Thamara Nishida Xavier da Silva,³ Ancely Ferreira dos Santos,³ Laura Mosteo,^{4,5} Colin R. Goding,⁴ José Pedro Friedmann Angeli,³ and Svenja Meierjohann^{1,6,7,*}

¹Institute of Pathology, University of Würzburg, 97080 Würzburg, Germany

²Department of Biochemistry and Molecular Biology, University of Würzburg, 97074 Würzburg, Germany

³Rudolf-Virchow Center for Integrative and Translational Bioimaging, University of Würzburg, 97080 Würzburg, Germany

⁴Ludwig Institute for Cancer Research, Nuffield Department of Medicine, University of Oxford, Oxford OX3 7DQ, UK

⁵Instituto de Investigação e Inovação em Saúde (i3S), Universidade do Porto, 4200-135 Porto, Portugal

⁶Comprehensive Cancer Center Mainfranken, University Hospital Würzburg, 97080 Würzburg, Germany

⁷Lead contact

*Correspondence: svenja.meierjohann@uni-wuerzburg.de

<https://doi.org/10.1016/j.celrep.2023.112724>

SUMMARY

The redox regulator NRF2 becomes activated upon oxidative and electrophilic stress and orchestrates a response program associated with redox regulation, metabolism, tumor therapy resistance, and immune suppression. Here, we describe an unrecognized link between the integrated stress response (ISR) and NRF2 mediated by the ISR effector ATF4. The ISR is commonly activated after starvation or ER stress and plays a central role in tissue homeostasis and cancer plasticity. ATF4 increases NRF2 transcription and induces the glutathione-degrading enzyme *CHAC1*, which we now show to be critically important for maintaining NRF2 activation. In-depth analyses reveal that NRF2 supports ATF4-induced cells by increasing cystine uptake via the glutamate-cystine antiporter xCT. In addition, NRF2 upregulates genes mediating thioredoxin usage and regeneration, thus balancing the glutathione decrease. In conclusion, we demonstrate that the NRF2 response serves as second layer of the ISR, an observation highly relevant for the understanding of cellular resilience in health and disease.

INTRODUCTION

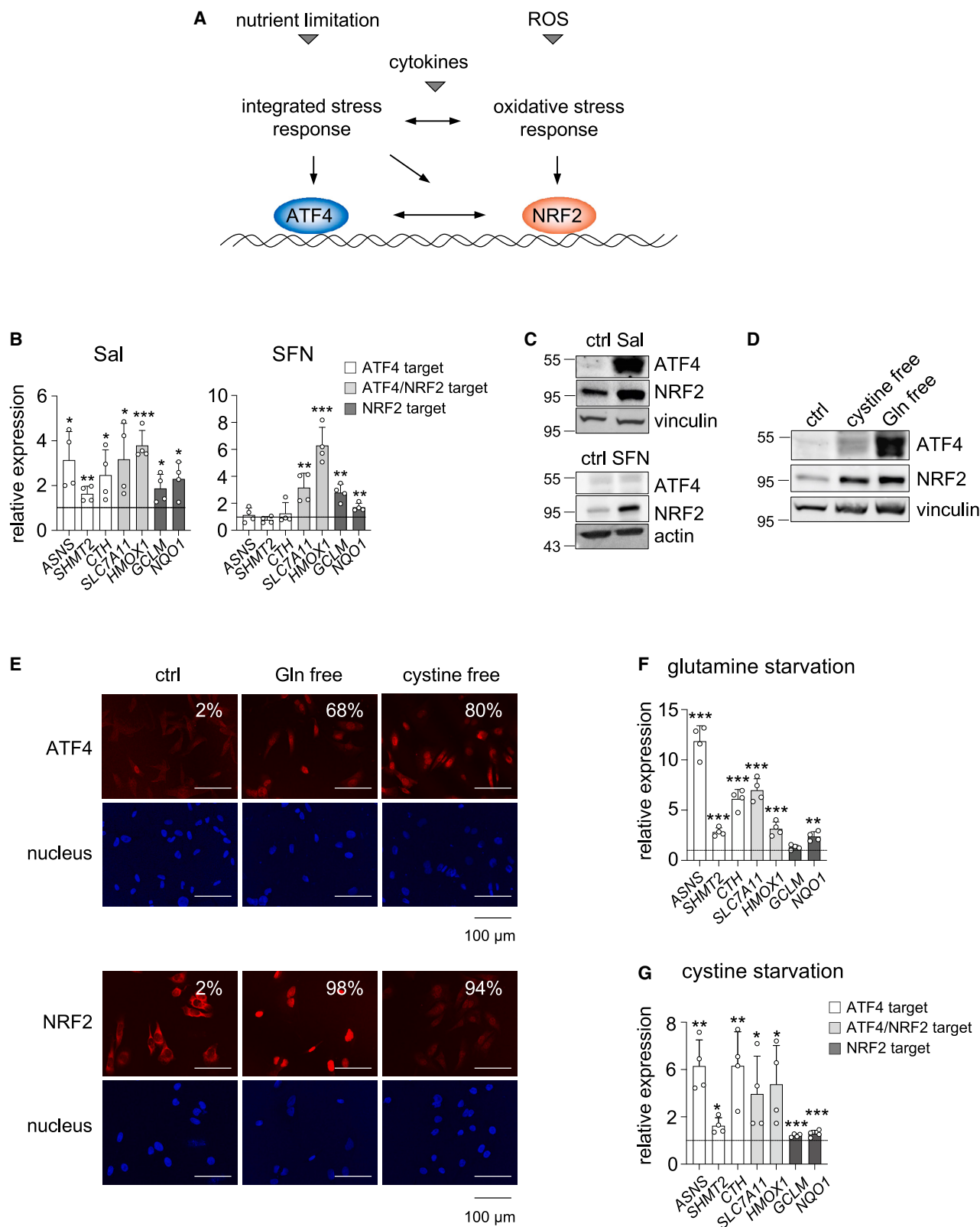
Adaptation to challenging conditions is an intrinsic cellular feature and is required to enable cellular plasticity and survival. As a result of their enhanced proliferation, altered metabolic activity, and the capability to invade new microenvironments, cancer cells take particular advantage of adaptation strategies for their own benefit. During cancer growth and metastasis, tumor cells will most likely encounter nutrient limitations and oxidative stress, thereby triggering a distinct set of cellular responses.¹

Specifically, the integrated stress response (ISR) plays a central role, as it directs different stress signals into one pathway via different eIF2 α kinases serving as stress sensors. Amino acid starvation leads to the accumulation of uncharged tRNAs, thereby activating general control non-derepressible 2 (GCN2).² Hypoxia, oxidative stress, or lactate accumulation can, among others, cause the aggregation of unfolded proteins, thereby generating endoplasmic reticulum (ER) stress and activating the PKR-like ER kinase (PERK) as a result.³ Furthermore, infection with double-stranded RNA viruses or heme depletion in erythroid cells lead to the activation of protein kinase R (PKR) and heme-regulated inhibitor (HRI), respectively.² All four kinases catalyze the phosphorylation of eIF2 α on serine 51, causing a block of cap-

dependent translation. Some genes, however, are selectively translated under these conditions, most prominently activating transcription factor 4 (ATF4), where the limited availability of the ternary complex allows longer ribosomal scanning and translation of the active protein.² ATF4 controls the expression of a large set of genes involved in amino acid uptake or synthesis⁴ and is instrumental for the expression of autophagy-related genes.⁵ Because of its activation by GCN2, PERK, and PKR as well as HRI, ATF4 is considered as an indicator protein for the activated ISR.

In addition, the oxidative stress response mediated by nuclear factor erythroid 2-related factor 2 (NFE2L2 or commonly NRF2) plays an important role in cellular adaptation. NRF2 is a short-lived protein which is, in contrast to ATF4, permanently synthesized but is quickly degraded in the absence of oxidative stress. The NRF2 interaction partner Kelch-like ECH-associated protein 1 (KEAP1) binds to NRF2 in the cytosol and serves as adapter between NRF2 and the CUL3/RBX ubiquitin ligase complex, leading to the proteasomal degradation of NRF2.^{6,7} Under conditions of oxidative or electrophilic stress, KEAP1 is modified at several cysteine residues, weakening its interaction with NRF2 and finally resulting in nuclear accumulation of NRF2.⁸ Here, NRF2 induces the transcription of genes containing an antioxidant response element.^{9,10}





(legend on next page)

A number of studies have demonstrated that ATF4 and NRF2 are both activated under similar stress conditions and in multiple cancer entities. This has been generally accepted because of the fact that oxidative stress and ER stress are closely connected and can cause or enhance each other.¹¹ For example, the ER-stress-responsive kinase PERK is able to phosphorylate NRF2, resulting in a weakened NRF2/KEAP1 interaction and activation of NRF2.¹² Contrarily, there is also evidence for an influence of NRF2 on the ISR/ATF4 pathway. In non-small cell lung cancer (NSCLC), activated NRF2 triggers asparagine and serine biosynthesis in an ATF4-dependent manner.^{13,14} In melanoma, NRF2 effectively induces expression of *PTGS2*, the gene encoding cyclooxygenase-2, by an indirect mechanism dependent on ATF4.¹⁵ However, it is unclear whether the crosstalk between ATF4 and NRF2 is a general phenomenon or can only occur under certain stress conditions.

Here we demonstrate interdependence between both transcription factors, thereby revealing that ATF4 activation is invariably linked to NRF2 activation. ATF4 ensures elevated NRF2 levels by deploying two mechanisms: (1) the transcriptional induction of *NFE2L2* expression and (2) metabolic regulation mediated by CHAC1-dependent depletion of intracellular glutathione (GSH). Consequently, ATF4 induction by the ISR guarantees the parallel induction of an NRF2-driven antioxidant response while supporting ATF4-dependent cysteine supply.

RESULTS

Joint activation of ATF4 and NRF2 by glutamine and cystine limitation

Events triggering the integrated or oxidative stress response occur frequently during tumor growth and metastasis. Nutrient limitation, reactive oxygen species (ROS), and cytokines are common challenges in the primary or metastatic tumor niche^{16–20} and are reportedly involved in the activation of ATF4 and NRF2^{15,21–24} (Figure 1A). Both transcription factors also play a role in therapy-induced stress, as shown in several studies where melanomas were treated with mitogen-activated protein kinase (MAPK) pathway inhibitors.^{25–27} Notably, MAPK-pathway-targeting therapy of melanomas leads to the selection of so-called persisters or escapees, which are capable of outlasting therapy.^{27,28} Yang and colleagues have previously identified a 40-gene set in single-cell analyses from melanoma escapees, which endured dabrafenib-induced stress and showed a distinct ATF4 signature.²⁷ Re-analysis of this gene set revealed a concurrent accumulation of numerous NRF2

target genes (Figure S1), implying that ATF4 and NRF2 might be jointly active under therapy stress.

To unravel the nature of the interaction between ATF4 and NRF2, we initially selected a set of bona fide indicator genes for NRF2 (*NQO1*, *GCLM*), ATF4 (*ASNS*, *SHMT2*, *CTH*), and joint NRF2/ATF4 (*HMOX1*, *SLC7A11*) transcriptional activity. All target genes were bound by NRF2 and/or ATF4 at their respective promoter regions in melanoma cells (Figure S2A).

As a proof of concept, ATF4 and NRF2 indicator genes were tested by specific inducers of the ISR and the oxidative stress response, respectively, in UACC-62 melanoma cells. The eIF2 α phosphatase inhibitor salubrinal results in the induction of the ISR, and consequently ATF4²⁹ and was accompanied by an elevation of all described ATF4 target genes but also of the NRF2-specific genes in this gene set (Figure 1B). In line with this, protein levels of ATF4 and NRF2 were strongly increased (Figure 1C). In contrast, sulforaphane (SFN), a well-documented NRF2 activator,³⁰ increased the expression of all tested NRF2 target genes and specifically increased NRF2 but not ATF4 protein (Figures 1B and 1C).

To monitor joint ATF4 and NRF2 activation, we chose starvation stress because of its high impact in the tumor niche and mimicked it by depleting glutamine or cystine for 24 h. By limiting amino acid availability for translation and GSH synthesis, both amino acid restrictions are able to cause the ISR as well as the oxidative stress response. Indeed, we observed an increase of NRF2 and ATF4 levels under both conditions by western blot (Figure 1D). Confocal fluorescence imaging revealed a high percentage of nuclear localization of both transcription factors after cystine and glutamine starvation (Figure 1E). This was generally confirmed in M14 melanoma cells by protein blot and standard immunofluorescence (Figures S2B and S2C). In addition, all ATF4 and NRF2 indicator target genes were increased to some extent, although *GCLM* induction was generally low and only reached significance under conditions of cystine starvation (Figures 1F and 1G). We therefore analyzed the expression of *TXNRD1* and *AKR1C3*, two additional well-characterized NRF2 target genes,^{31–33} and again observed an induction after salubrinal and sulforaphane treatment as well as cystine and glutamine withdrawal (Figures S3A and S3C). To identify the best condition for establishing a robust stress response, a time-course experiment was carried out for UACC-62 melanoma cells cultivated in glutamine-free medium, as glutamine starvation had the strongest effect on both transcription factors. After 2 h of glutamine starvation, ATF4 and NRF2 levels had already increased strongly (Figure S3B) and still remained elevated at 24 h. Gene expression analysis of early (2 h), intermediate (8 h), and late (24

Figure 1. Coactivation of the integrated and oxidative stress responses

- (A) Scheme of common joint triggers of the ISR and the oxidative stress response and their downstream transcription factors ATF4 and NRF2.
(B) Left: real-time PCR analysis of ATF4, NRF2, or joint target genes after salubrinal (Sal) treatment (20 μ M, 24 h) and sulforaphane treatment (7.5 μ M, 24 h) in UACC-62 human melanoma cells (n = 4).
(C) Corresponding immunoblot, showing ATF4 and NRF2 expression. Vinculin or actin was used as loading control.
(D) Immunoblot of ATF4 and NRF2 in UACC-62 cells after cultivation in cystine-free or glutamine-free medium for 24 h. Vinculin served as loading control.
(E) Corresponding confocal fluorescence images of ATF4 or NRF2 (red) in UACC-62 cells after glutamine or cystine starvation for 24 h. Hoechst 33342 (blue) was used for nuclear staining. Representative images are shown. To calculate the percentage of cells with ATF4 and NRF2 nuclear localization, 50 cells from each condition were counted. Images were taken with a confocal laser scanning microscope (Leica TCS SP2) with a 20 \times objective. Scale bars, 100 μ m.
(F and G) Corresponding real-time PCR analysis of UACC-62 cells kept in glutamine-free (F) or cystine-free (G) medium (n = 4).
In (B), (F), and (G), error bars represent SD. The dotted lines visualize the respective control. For each gene, unpaired two-sided t test was carried out (*p < 0.05, **p < 0.01, ***p < 0.001).

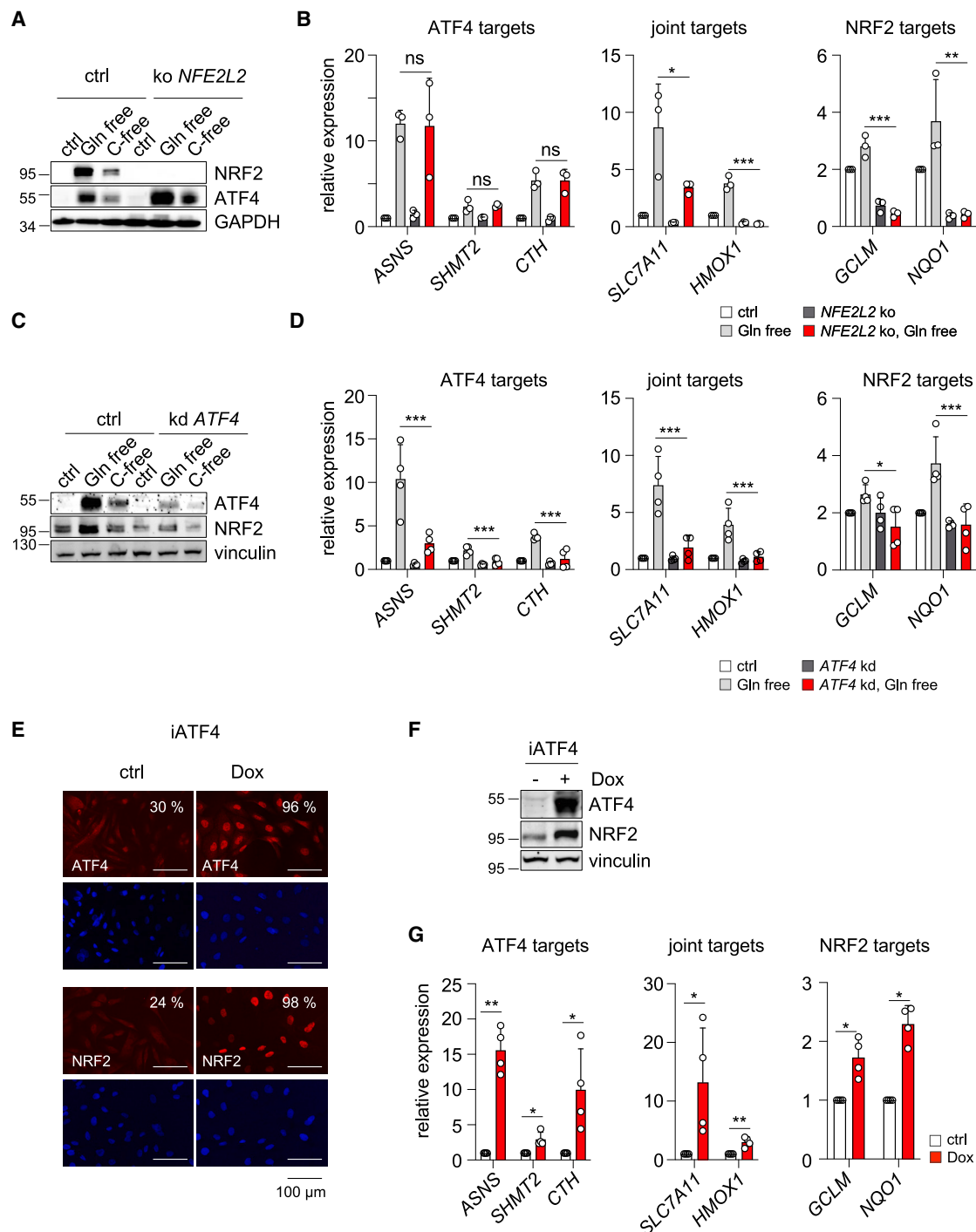


Figure 2. ATF4 regulates NRF2 target genes

(A) Western blot analysis of NRF2 and ATF4 in UACC-62 non-target and *NFE2L2*-KO cells kept in glutamine-free, cystine-free, or reconstituted control medium for 24 h. GAPDH served as loading control.

(B) Corresponding real-time PCR analysis showing induction of specific ATF4 or NRF2 target genes or joint target genes, respectively, under conditions of glutamine withdrawal (24 h) in non-target control or *NFE2L2*-KO cells ($n = 3$). Data were normalized to the untreated non-target control.

(C) Western blot analysis of NRF2 and ATF4 in UACC-62 non-target and *ATF4*-KD cells kept in glutamine-free, cystine-free, or reconstituted control medium for 24 h. Vinculin served as loading control.

(D) Corresponding real-time PCR analysis showing induction of specific ATF4 or NRF2 target genes or joint target genes, respectively, under conditions of glutamine withdrawal (24 h) in non-target control or *ATF4*-KD cells ($n = 4$). Data were normalized to the untreated non-target control.

(legend continued on next page)

h) time points showed that the most robust induction of all target genes was reached after extended glutamine withdrawal. This condition was chosen for the subsequent studies.

ATF4 acts as an obligatory NRF2 inducer

After establishing suitable indicator genes for ATF4 and NRF2, their expression was tested in UACC-62 melanoma cells deficient for NRF2 or ATF4. After NRF2 knockout (*NFE2L2*-KO), NRF2 protein expression was not visible even after glutamine or cystine withdrawal (Figures 2A and S10A). In response to glutamine withdrawal, the expression of joint ATF4/NRF2 targets and NRF2 targets was suppressed in the NRF2-KO cells, while ATF4 target genes were unaffected (Figures 2B and S3D). Similar results were gained with an independent NRF2-KO clone (Figures S3E, S3F, and S10A). The generation of ATF4-KO clones was more difficult, as it was only possible in our hands to generate UACC-62 cell clones with reduced ATF4 (ATF4 knockdown: ATF4-KD). This is in accordance with public data of Cancer Cell Line Encyclopedia (CCLE) cell lines, where ATF4 is identified as “common essential” gene with strongly negative CRISPR dependency score in contrast to NRF2 (Figure S4A, data derived from <https://depmap.org/portal/>)³⁴. However, sequencing revealed frame shifts and splice mutations of the targeted ATF4 gene regions in both alleles (Figure S10B). As ATF4 protein induction was strongly impaired after glutamine or cystine withdrawal (Figures 2C and S4C), it is possible that the antibody recognized lower amounts of an altered ATF4 version. Interestingly, all glutamine-starvation-inducible ATF4 and NRF2 target genes exhibited reduced activation in these ATF4-KD cells (Figures 2D, S4B, and S4D). In addition, NRF2 protein levels were lower when ATF4 was depleted (Figures 2C and S4C). To test whether this can be phenocopied in an independent cell line, we generated M14 melanoma cells with endogenous ATF4 knockout. Compared to the UACC-62, where low ATF4 levels were maintained, ATF4 was entirely blunted in M14 cells (Figure S4E). Again, ATF4 knockout had a strongly negative impact on NRF2 expression and activity (Figures S4E and S4F). These results suggest a critical role of ATF4 in mediating NRF2 activity under conditions of metabolic stress, while NRF2 is not required for ATF4 activity.

To investigate NRF2 activation by ATF4 in absence of confounding factors that might be associated with glutamine withdrawal, we used UACC-62 melanoma cells with doxycycline-inducible ATF4 (iATF4). Doxycycline was applied for 3 days to mimic extended stress.¹⁵ Intriguingly, ATF4 expression was associated with a strong nuclear translocation as well as an enhanced expression of NRF2 (Figures 2E, 2F, and S4G). Increased expression of ATF4 and NRF2 target genes was also observed (Figure 2G), indi-

cating that ATF4 directly stimulates NRF2 levels and transcriptional activity.

In the absence of exogenous stress, NRF2 has a short half-life of 15–20 min, as it is strongly regulated at the protein level. To test whether ATF4 increases the half-life of NRF2, we induced ATF4 in the presence of cycloheximide for up to 120 min to prevent *de novo* protein translation. Although NRF2 levels were strongly increased in the presence of ATF4, NRF2 half-life was not altered (Figure 3A). Conversely, ATF4 knockdown reduced the overall levels of NRF2 in glutamine-starved melanoma cells but did not affect NRF2 half-life (Figure S4H). ATF4 was also degraded at a comparable rate, leading to the conclusion that NRF2 levels were elevated as long as ATF4 was present. As a transcription factor, ATF4 recognizes distinct amino acid response elements (AARE), and it was previously described that the *NFE2L2* promoter contains an AARE site, which is bound by ATF4 after ER stress.³⁵ Chromatin immunoprecipitation sequencing (ChIP-seq) data from melanoma cells revealed four more ATF4 binding sites, which were located in the promoter and first intron of *NFE2L2*. Three of the five binding sites contained AARE sites (marked with asterisks in Figure 3B) and all could be confirmed in an independent ChIP in UACC-62 iATF4 cells (Figure 3C), strongly implying that *NFE2L2* serves as a bona fide target gene of ATF4. Indeed, *NFE2L2* expression was increased in response to several ATF4 triggers, including doxycycline-inducible ATF4, glutamine starvation, and salubrinal (Figures 3D–3F). In all cases, this went along with increased NRF2 protein expression (Figures 1C, 1D, and 2F). To test whether the coregulation of ATF4 and NRF2 also occurs *in vivo*, we analyzed a publicly available microarray dataset of murine melanomas that underwent adoptive T cell transfer and are subject to high levels of cytokine stress,²⁰ as it was previously reported that ATF4 is strongly induced in this mouse model early during treatment (EDT) as well as in melanomas relapsing from T cell therapy (R).^{21,36} Next to *Atf4* and its target gene *Asns*, we also detected a profound upregulation of *Nfe2l2* and the joint ATF4/NRF2 target gene *Slc7a11* in EDT and R samples (Figures 3G and 3H). Although these data cannot reveal causal events, they show that coregulation of both factors occurs under stress conditions *in vivo*.

ATF4 causes CHAC1-dependent GSH degradation

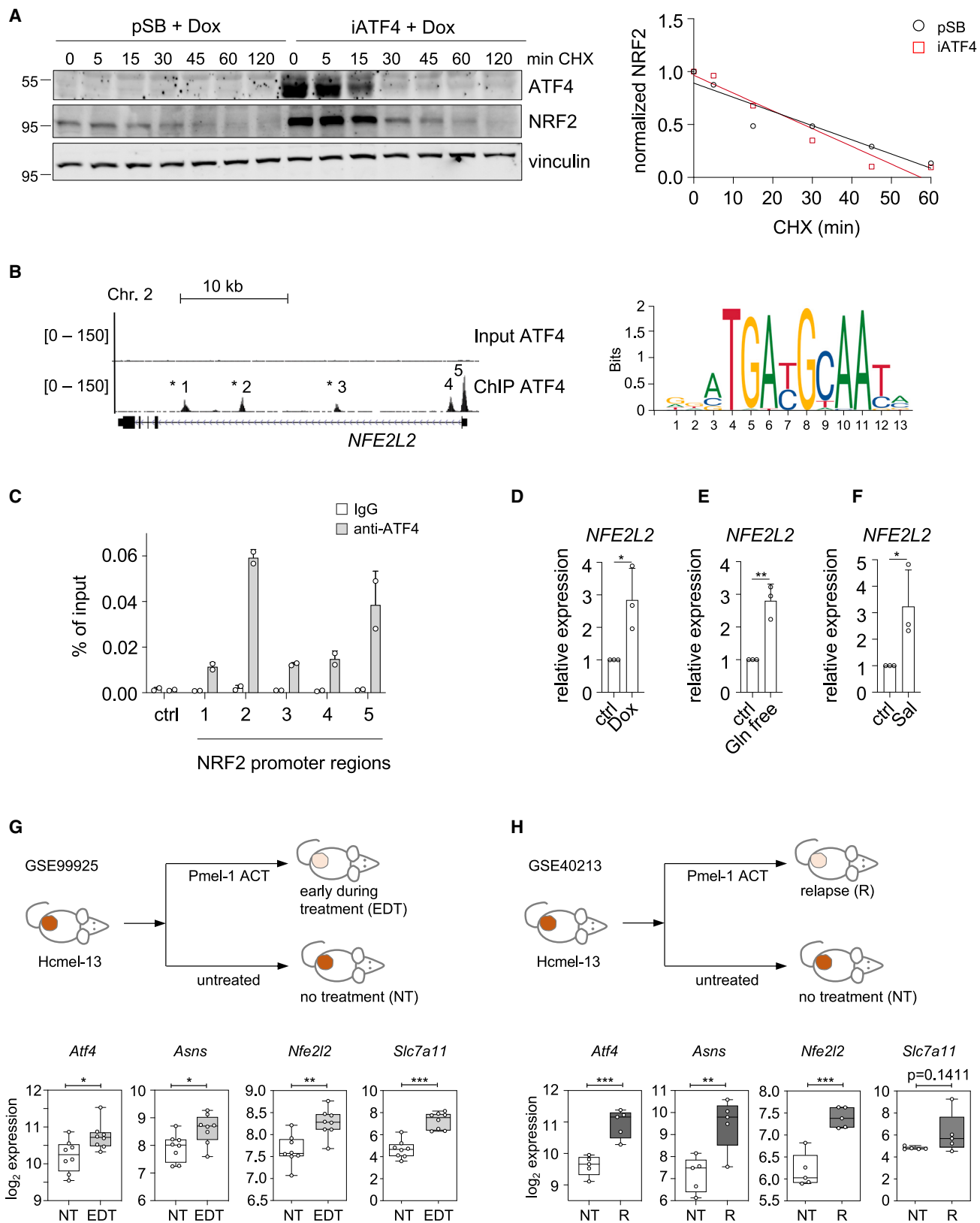
Despite the observed transcriptional induction, the major regulation of NRF2 is expected to occur post-transcriptionally.³⁸ We therefore investigated whether ATF4 adds another layer of NRF2 regulation independent of *NFE2L2* transcription. As ATF4 plays a prominent role in metabolic adaptation to stress and NRF2 is responsive to a number of metabolites, we performed mass spectrometry analyses of water-soluble metabolites after doxycycline-induced ATF4 expression in UACC-62

(E) Left: representative confocal fluorescence images of ATF4 or NRF2 (red) in UACC-62 cells transfected with the doxycycline (Dox)-inducible ATF4 expression vector pSB-ATF4 (iATF4). Cells were incubated with or without 100 ng/mL Dox for 3 days. Hoechst 33342 (blue) was used for nuclear staining. Images were taken with a confocal laser scanning microscope (Leica TCS SP2) with a 20× objective. Scale bars, 100 μm. To calculate the percentage of cells with ATF4 and NRF2 nuclear localization, 50 cells from each condition were counted.

(F) Corresponding western blot, using vinculin as loading control.

(G) Real-time PCR analysis showing induction of ATF4 or NRF2 target genes in response to 100 ng/mL Dox in iATF4 UACC-62 (3 days) (n = 4). Data were normalized to the Dox-free control conditions.

In (B), (D), and (G), error bars represent SD. Significance was calculated by one-way ANOVA with Dunnett’s multiple comparison test (*p < 0.05, **p < 0.01, ***p < 0.001).



(legend on next page)

cells. We found characteristic changes in amino acids and small peptides, where asparagine strongly increased while other amino acids (glutamate, aspartate, lysine, arginine) slightly decreased after 1 day of ATF4 induction. At the same time, levels of the antioxidant tripeptide GSH were strongly diminished (Figure 4A). The reduction of GSH was even more pronounced when ATF4 was induced for an extended time period of 3 days (Figure S5A) and was confirmed by an independent assay³⁹ (Figures 4B and 4C). Analysis of earlier time points showed that GSH levels started to decrease after 8 h of ATF4 induction (Figures S5B and S5C). Notably, levels of intracellular oxidized GSH (GSSG) were negligibly low under all tested conditions. As GSH depletion, e.g., by inhibition of GSH biosynthesis with the glutamyl cysteinyl ligase (GCL) inhibitor buthionine sulfoximine (BSO), can induce NRF2⁴⁰ (Figures S5D and S5E), we presumed that ATF4 mediates NRF2 activation via this mechanism. To identify potential mediators of ATF4-dependent GSH reduction, RNA-sequencing data from 501mel melanoma cells treated with salubrinal were reanalyzed, considering genes from the Kyoto Encyclopedia of Genes and Genomes (KEGG) gene set “GSH metabolism.” Here, the γ -glutamylcyclotransferase *CHAC1* stood out, as it was strongly induced after all tested salubrinal treatment conditions²¹ (Figure 4D, left). Similar results were obtained using an RNA-sequencing dataset of control and *Atf4*-KO mouse embryonic fibroblasts (MEFs) treated with tunicamycin, which activates ATF4 via ER stress.⁴¹ Here, the tunicamycin-induced *CHAC1* expression was entirely prevented in *Atf4*-KO cells (Figure 4D, right). *CHAC1* specifically cleaves GSH into cysteinylglycine and 5-oxoproline, which can be subsequently converted to glutamate (Figure 4E, upper panel). ATF4 binds to the promoter of *CHAC1*, which contains the AARE sequence 5'-TGATGCAAT-3', as confirmed by ChIP-seq data with 501mel cells (Figure 4E, lower panel). Intriguingly, analysis of CCLE cancer cell lines, representing cell lines from different cancer entities, revealed *CHAC1* as the gene with the strongest positive correlation to ATF4 expression (Figure 4F). Consequently, ATF4 induction in UACC-62 iATF4 melanoma cells led to elevated *CHAC1* RNA and protein expression (Figures 4G and 4H). *CHAC1* was slightly more stable than ATF4 and NRF2 after cycloheximide treatment but was highest when NRF2 showed the strongest stabilization (Figure S5F).

CHAC1 may therefore serve as an NRF2 activator downstream of ATF4. To test this hypothesis, we generated melanoma

cells lacking *CHAC1*. Strikingly, *CHAC1* deficiency led to a pronounced accumulation of GSH in normal medium, approximately 8-fold higher compared to the control (Figure 5A). Under conditions of glutamine starvation, GSH levels were lowered but still remained more than 2-fold elevated compared to untreated control cells. Curiously, loss of *CHAC1* was sufficient to fully prevent the stabilization of NRF2 upon ATF4 induction (Figure 5B). When *CHAC1* was overexpressed for an extended time span, this led to a pronounced GSH depletion and NRF2 induction even in absence of additional metabolic stress (Figures 5C, 5D, S5G, and S5H). *CHAC1* was also targeted by CRISPR-Cas9 in iATF4 melanoma cells, which resulted in a partial knockout (Figure 5E). As a result, the increase and cellular localization of NRF2 was impaired (Figure 5F), leading to the conclusion that *CHAC1* serves as a major effector of ATF4-dependent NRF2 activation.

To test whether the activation of NRF2 by ATF4 is a general consequence of the integrated stress response, we used two additional ISR triggers as well as cell lines from different lineages. Next to the already described glutamine withdrawal (which activates the GCN2 kinase), BTdCPU, an activator of HRI, as well as the PERK activator tunicamycin, leads to very efficient ATF4 and NRF2 stabilization in UACC-62 melanoma cells (Figures S6A and S6B). In addition, transcript levels of *NFE2L2*, *CHAC1*, and NRF2 target genes were upregulated under these conditions (Figures S6E–S6G). Similar results were obtained with the lung adenocarcinoma cell line H23 and the breast cancer cell line MDA-MB-468, in which NRF2 was stabilized and at least two out of three NRF2 target genes were upregulated under conditions of ISR-causing stress (Figures S6C–S6G). The only exception was observed for glutamine-starved MDA-MB-468 cells, which tolerated this condition rather well and only showed a mild induction of both ATF4 and NRF2.

In conclusion, ATF4-dependent NRF2 activation is an obligatory and widespread consequence of ISR-induced stress.

Metabolic connections between ATF4 and NRF2

To better understand the cellular advantage of ATF4-dependent NRF2 activation, we performed metabolic tracing with ¹³C-labeled glutamine, which was added to NRF2-proficient or -deficient iATF4 cells for 4 h. ¹³C incorporation into metabolites was analyzed for intracellular metabolites as well as cell-culture supernatants, and ATF4 was induced for 3 days prior to ¹³C labeling (Figures 6A and 6B). [¹³C]Glutamine uptake was similar in

Figure 3. ATF4 induces NRF2 transcription

(A) Left: western blot analysis of NRF2 and ATF4 in UACC-62 control (pSB) or ATF4-inducible cells (iATF4) treated with doxycycline (Dox; 100 ng/mL) for 1 day. Cycloheximide (CHX; 5 μ g/mL) was added to the medium for indicated time points. Right: NRF2 protein amount was quantified using the Fiji gel analyzer tool (ImageJ) and normalized to the loading control vinculin. This value was set as 1 for the CHX-free condition of each cell line (pSB and iATF4, respectively) and was used as reference for the ensuing CHX treatments.

(B) Left: genome browser tracks of the *NFE2L2* gene with ATF4 binding, evaluated by ATF4 ChIP-seq analysis in human 501mel melanoma cells and an input control. Right: enriched sequence pattern in the region of the ATF4 binding site. The matrix profile was created in JASPAR 2020.³⁷

(C) Validation of ATF4 binding to *NFE2L2* by ChIP in UACC-62 iATF4 cells after ATF4 induction (100 ng/mL, 3 days).

(D–F) Real-time PCR showing *NFE2L2* gene expression in UACC-62 cells (D) upon induction of ATF4 in UACC-62 pSB-ATF4 cells (3 days, 100 ng/mL Dox, n = 3), (E) after glutamine starvation for 24 h (n = 3), and (F) in response to salubrinal treatment (20 μ M, 24 h, n = 3). Error bars indicate SD. Significance was calculated by unpaired two-sided t test (*p < 0.05, **p < 0.01).

(G and H) Scheme of adoptive T cell transfer in transplanted HcMel3 murine melanomas, as published previously.^{20,21} Tumors of untreated mice (NT) and mice early during treatment (EDT) (G) or untreated mice (NT) and mice relapsed after T cell therapy (R) (H) were subjected to microarray analysis, as deposited under accession numbers GEO: GSE99925 and GSE40213, respectively. Box and whiskers plots show the expression of *Atf4*, *Asns*, *Nfe2l2*, and *Slc7a11* in the respective tumors. An unpaired two-sided t test was performed for statistical analysis (*p < 0.05, **p < 0.01, ***p < 0.001).

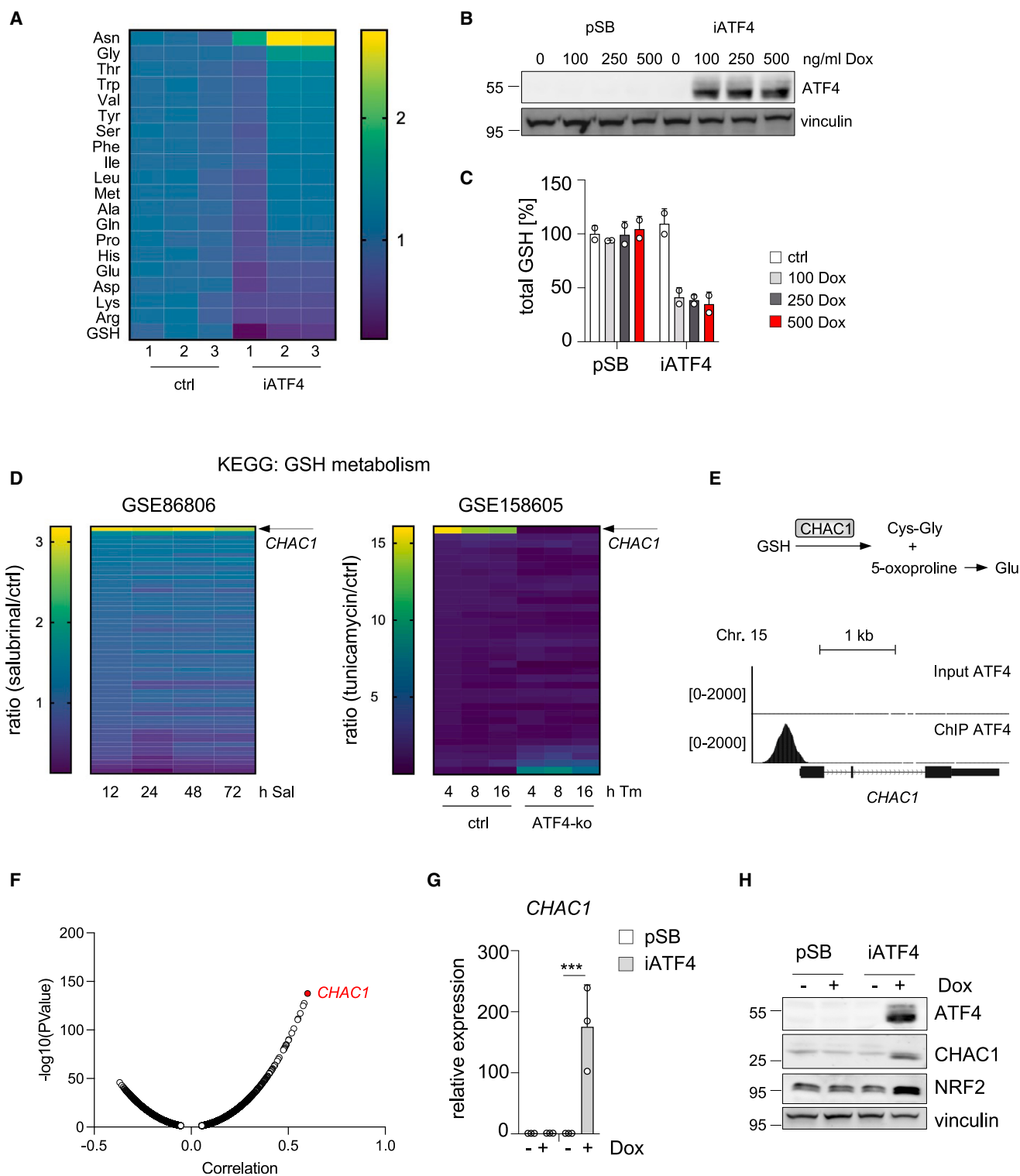


Figure 4. ATF4 activation causes glutathione depletion

(A) Heat plot showing the changes in amino acids and glutathione (GSH) in UACC-62 control cells (pSB) and iATF4 cells after doxycycline (Dox) induction (100 ng/mL, 24 h). The graph shows the ratio of Dox versus untreated condition. Mass spectrometry analyses were carried out in triplicates for each condition. (B) Immunoblot of ATF4 in UACC-62 pSB and iATF4 cells in response to indicated concentrations of Dox. Vinculin served as loading control.

(legend continued on next page)

iATF4 as well as *NFE2L2*-KO iATF4 cells, irrespective of ATF4 induction (Figure S7A). A large fraction of aspartate was labeled with four ^{13}C atoms (m+4), demonstrating a fast metabolism of glutamine via glutamate to aspartic acid. This was further increased after ATF4 induction and was comparable under control and *NFE2L2*-KO conditions. An increased fraction of m+4 asparagine was also observed after ATF4 induction irrespective of the NRF2 status, reflecting the activity of the ATF4 target ASNS. Furthermore, m+4 succinate and m+4 malate increased after ATF4 induction in NRF2-proficient and -deficient cells (Figure S7A). These data show that ATF4 increases the utilization of glutamine for aspartate/asparagine synthesis as well as the citric acid cycle. Interestingly, despite the overall reduction in GSH (Figure 6C, left), the fraction of m+5-labeled intracellular GSH also increased strongly after doxycycline-mediated ATF4 induction, indicating high *de novo* GSH synthesis. This increase was less pronounced in *NFE2L2*-KO cells (Figure 6C [right] and Figure S7A). As it was unexpected that the overall GSH levels were almost unaffected in *NFE2L2*-KO cells despite reduced GSH synthesis, we monitored GSH export by measuring GSSG in the medium, where GSH is present in its oxidized form due to the pro-oxidant extracellular conditions. We observed a tendency for lower medium GSSG levels and therefore GSH export in NRF2-deficient cells, providing a possible explanation for the relative maintenance of intracellular GSH levels compared to control cells (Figure S7B).

Thus, the ATF4-mediated reduction of intracellular GSH was counteracted by *de novo* GSH synthesis, an effect supported by NRF2. The GSH pathway is strongly connected to the xCT antiporter system, a heterodimer of SLC7A11 and SLC3A2, which exports intracellular glutamate in exchange for extracellular cystine. ATF4 induction led to a strong induction of the extracellular m+5 glutamate/monoisotopic mass (MIM) glutamate ratio, indicating an export of previously metabolized glutamate (Figure 6D). In addition, cystine decreased in the medium of ATF4-treated cells, leading to a doxycycline/control ratio of 0.76. In *NFE2L2*-KO cells, the effect of ATF4 induction on glutamate export and cystine import was generally lower, with lower glutamate export and higher doxycycline/control ratio of extracellular cystine (Figure 6D). This speaks for a considerable contribution of NRF2 to ATF4-mediated xCT activity and is in line with the role of NRF2 in upregulating the xCT component *SLC7A11*. Accordingly, SLC7A11 protein expression was lower in ATF4-stimulated NRF2-deficient cells compared to NRF2-proficient controls, while ASNS levels were comparable (Figure 6B).

To test the involvement of CHAC1-dependent GSH depletion in xCT activation, control and *CHAC1*-deficient iATF4 cells were

treated with [^{13}C]glutamine for 4 h, as described above, and glutamate and cystine levels were measured in the supernatant. Similar to *NFE2L2*-KO cells, *CHAC1*-KO cells showed an impaired m+5 glutamate/MIM glutamate ratio and led to a less pronounced decrease of cystine after ATF4 induction (Figures 6E and 6F, summarized in Figure 6G). This reflects the dual role of CHAC1 in (1) providing GSH-derived glutamate as substrate for xCT and (2) activating NRF2 to elevate SLC7A11.

In summary, activated ATF4 taps the intracellular GSH pool in a CHAC1- and NRF2-dependent manner to enable sufficient cystine supply. Of note, ATF4 is also a transcriptional activator of the cysteinyl tRNA synthetase *CARS1*, which is induced NRF2 independently, thereby enabling cysteine incorporation into proteins and elevating cysteine requirement (Figure S8A). The depletion of GSH for the benefit of cysteine availability reduces cellular antioxidants that are required for intracellular redox reactions including the reduction of newly imported cystine to cysteine. However, cystine reduction can also be catalyzed by thioredoxin⁴³ (depicted in Figure 7A), which becomes more important when GSH is depleted. Several members of the thioredoxin system and the pentose phosphate pathway, which provides NADPH for thioredoxin regeneration, are NRF2 target genes, as shown earlier for *TXNRD1*. Accordingly, *NFE2L2*-KO cells are more sensitive to a combination of the GCL inhibitor BSO and the thioredoxin reductase inhibitor auranofin than control cells (Figure S8B). We therefore tested to what extent ATF4-dependent NRF2 induction affects the expression of *TXNRD1* (thioredoxin reductase 1), *TXN* (thioredoxin), *G6PD* (glucose-6-phosphate dehydrogenase), and *PGD* (phosphogluconate dehydrogenase). Glutamine starvation of UACC-62 cells for 1 day had no visible effect on the expression of *TXN* and *PGD*, although *NFE2L2*-KO cells showed lower expression of both genes under this condition (Figure S8C). However, both were upregulated after prolonged ATF4 induction for 3 days in an NRF2-dependent manner (Figure S8D). In addition, *TXNRD1* and *G6PD* increased significantly after glutamine starvation (Figure 7B) and doxycycline-inducible ATF4 stimulation (Figure 7D). This could be confirmed at the protein level except for G6PD in the case of glutamine starvation, suggesting that the accumulation of G6PD protein requires a longer ATF4 stimulus (Figures 7C and 7E). In the absence of NRF2, basal levels of *TXNRD1* and *G6PD* were lower, and their ATF4-dependent upregulation was entirely prevented (Figures 7B–7E).

In conclusion, these data show that the coupling of ATF4 to NRF2 enhances: (1) cysteine availability by supporting xCT activity and (2) antioxidant capacity by increasing enzymes of the thioredoxin and pentose phosphate pathways (Figure 7F). Accordingly,

(C) Corresponding GSH levels measured by Tietze assay. The assay was performed twice, each time in duplicates.

(D) Heat plots showing gene expression of the KEGG gene set “GSH metabolism” in 501mel melanoma cells treated with salubrinal (Sal, left) or control and *Atf4*-KO MEFs treated with tunicamycin (Tm, right) for indicated time points. Data show the ratio of treated versus untreated condition and are derived from GEO: GSE86806, previously published by Falletta and colleagues,²¹ and GEO: GSE158605, published by Torrence et al.⁴¹

(E) Upper image: reaction catalyzed by CHAC1. Lower image: genome browser tracks of the *CHAC1* gene with ATF4 binding, evaluated by ATF4 ChIP-seq analysis in human 501mel melanoma cells and an input control.

(F) ATF4 Pearson correlation analysis, using *ATF4* gene expression as dataslice and gene expression 22Q2 public data as dataset from all CCLE cell lines, as provided by the Cancer Dependency Map (<https://depmap.org/portal/>; <https://depmap.org/portal/ccle/>).⁴²

(G) Real-time PCR of *CHAC1* after Dox treatment (100 ng/mL, 3 days) in control or iATF4 UACC-62 cells (n = 3). Significance was calculated by one-way ANOVA with Dunnett’s multiple comparison test (***p < 0.01). Error bars indicate SD.

(H) Corresponding western blot of ATF4, CHAC1, and NRF2 with vinculin as loading control.

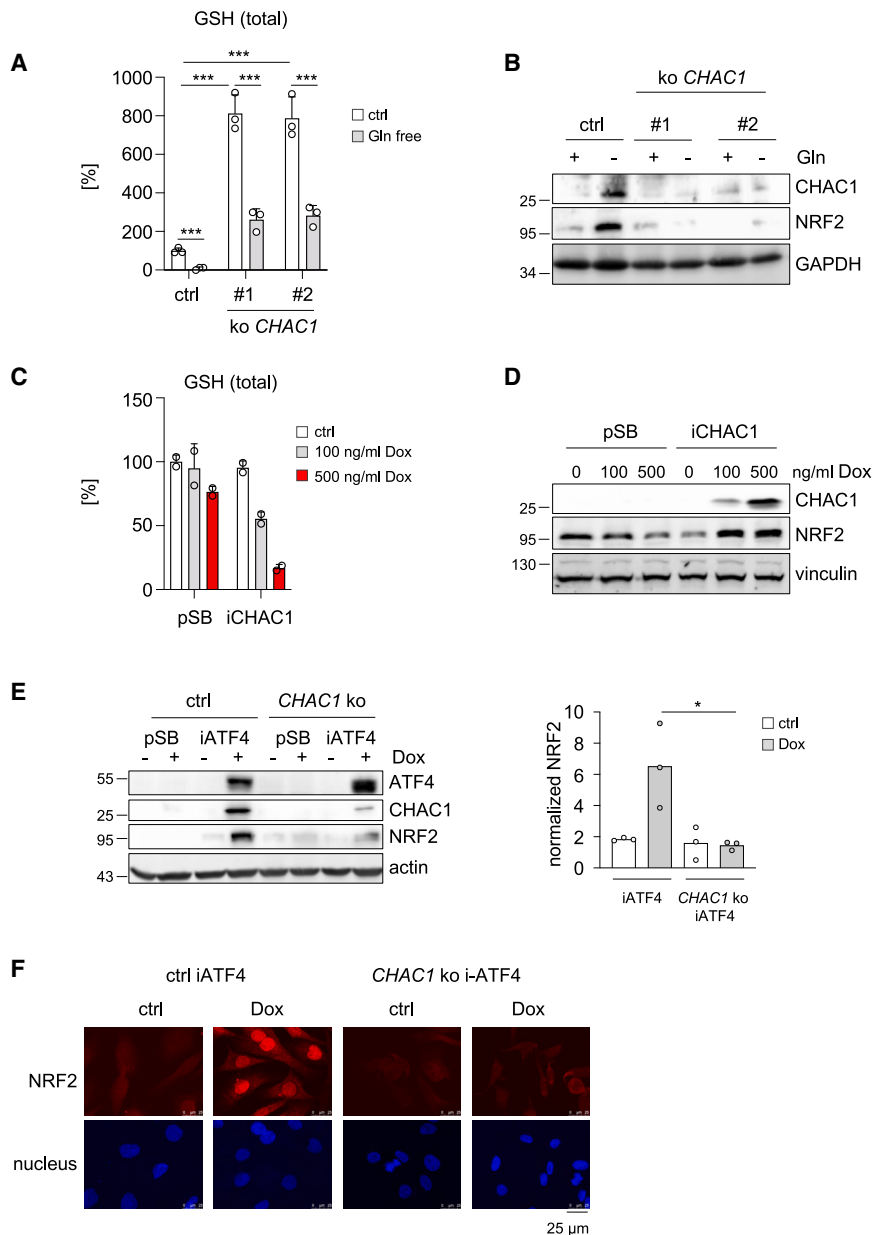


Figure 5. CHAC1 mediates glutathione depletion and NRF2 activation

(A) Relative concentration of total glutathione (GSH), measured by Tietze assay, in control UACC-62 cells (non-target gRNA) and two independent CHAC1-KO cell clones kept in control or glutamine-free medium for 24 h ($n = 3$). For statistical analysis, one-way ANOVA with Dunnett's multiple comparison test was applied ($***p < 0.001$). Error bars represent SD.

(B) Corresponding immunoblot of CHAC1 and NRF2. GAPDH served as loading control.

(C) Intracellular GSH concentration in pSB and pSB-CHAC1 transfected UACC-62 cells in response to doxycycline (Dox) with indicated concentrations for 7 days. The concentrations were measured by Tietze assay and were performed two times in duplicates. Error bars represent SD.

(D) Corresponding immunoblot of CHAC1 and NRF2 with vinculin as loading control.

(E) Left: western blot of ATF4, CHAC1, and NRF2 in UACC-62 control cells (non-targeting gRNA) or CHAC1-KO cells, each either transfected with empty vector (pSB) or iATF4 (pSB-ATF4). To induce ATF4 expression, 100 ng/mL Dox was applied for 3 days. Actin served as loading control. Right: quantification of NRF2 expression in iATF4 and CHAC1-KO iATF4 cells (UACC-62). NRF2 protein amount was quantified using the Fiji gel analyzer tool (ImageJ) and normalized to the loading control vinculin. Data are derived from three independent western blots. For statistical analysis, one-way ANOVA with Dunnett's multiple comparison test was applied ($*p < 0.05$).

(F) Corresponding immunofluorescence staining for NRF2 (red). Hoechst 33342 (blue) was used for nuclear staining. Representative images are shown. Images were taken with an inverted microscope (DMI 6000 B, Leica) with a 63 \times objective. Scale bars, 25 μ m.

NRF2-dependent cells are associated with improved tolerance toward the xCT inhibitor erastin and the thioredoxin inhibitor PX-12, as demonstrated by CRISPR dependency data from the depmap portal, representing all cancer cell lines with available inhibitor sensitivity data (Figure S8E). Similarly, high expression of the NRF2 target genes *SLC7A11* and *G6PD* correlate with higher tolerance toward these inhibitors (Figures S8F and S8G). This is consistent with the observation that NRF2-deficient melanoma cells are more sensitive to cystine depletion than their NRF2-proficient counterparts (Figure S8H). We next tested the hypothesis that NRF2 activation affects cellular resilience after ATF4 induction. Moderate ATF4 induction, as applied in previous experiments, decreased viability to approximately 50% (UACC-62) and 70% (M14) after 3 days (Figure S9A), which is expected because of

ATF4's antiproliferative effects in melanoma cells and other cell types.^{2,21} In contrast, ATF4 expression provided melanoma cells with a growth advantage in the presence of erastin, which is in accordance with the elevated xCT activity in ATF4 induced cells. In NRF2-KO cells, cellular viability after ATF4 induction was more strongly reduced (Figure S9B) and decreased further with increasing ATF4 dosage (Figure S9C). To test whether overactivated NRF2 has the contrary effect, the influence of KEAP1 was tested in the context of ATF4 activation. KEAP1 is considered as the major suppressor of NRF2 activity and is frequently mutated in NSCLC, resulting in permanently activated NRF2.⁴⁴ The NSCLC cell lines H23 and A549 contain wild-type and mutant KEAP1, respectively, leading to highly elevated NRF2 levels in the case of A549 cells (Figure S9D). The iATF4 construct was transfected into both cell lines. In both cases, ATF4 induction reduced intracellular GSH (Figure S9E). Interestingly, ATF4 only had a minor effect on KEAP1-mutant A549 cells but reduced viability of H23

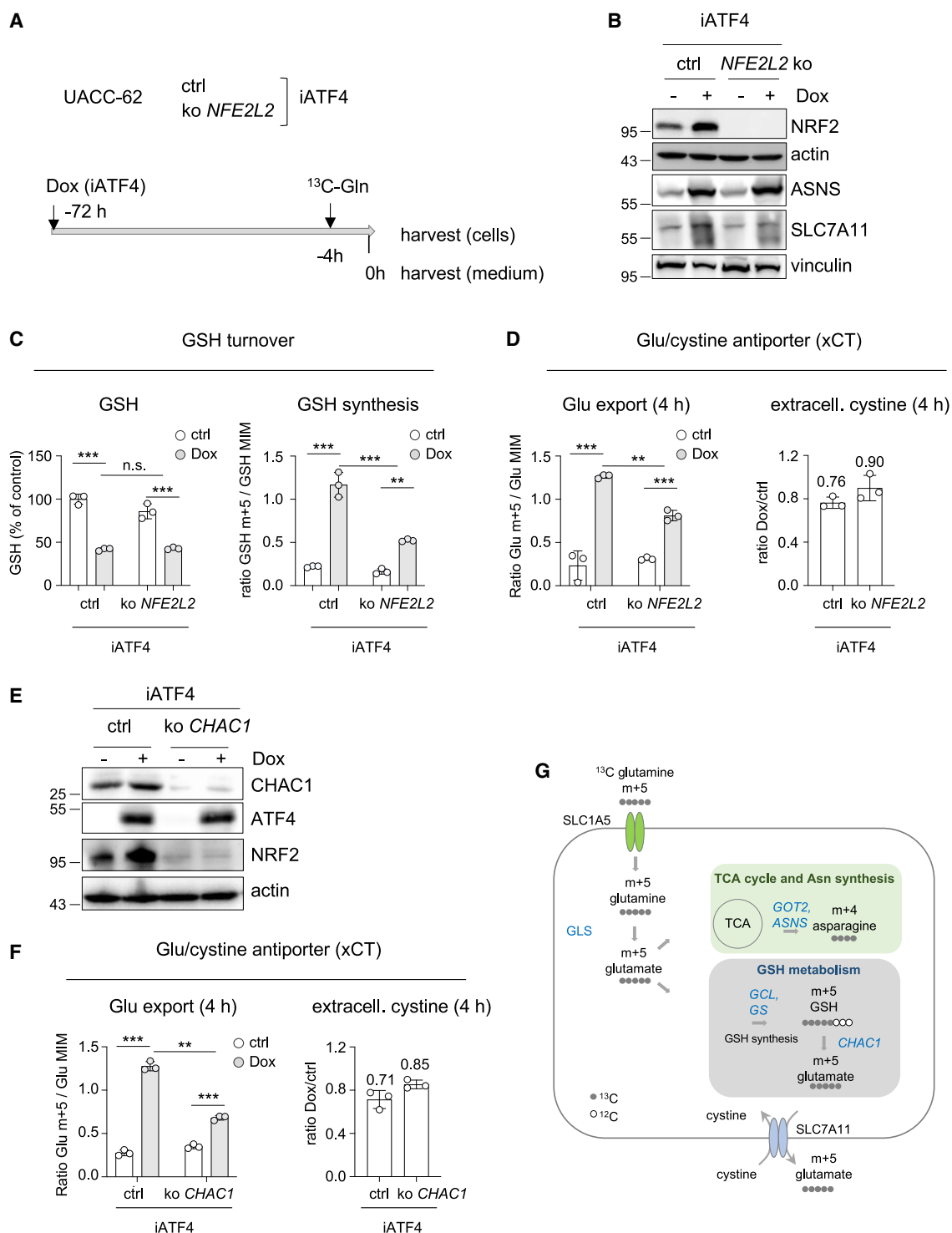


Figure 6. Metabolic changes after ATF4 induction

(A) Schematic representation of the metabolic tracing experiment using [^{13}C]glutamine.

(B) Protein blot showing NRF2, ASNS, and SLC7A11 expression in UACC-62 cells used for metabolic analyses after ATF4 induction (100 ng/mL doxycycline [Dox], 3 days). Actin or vinculin served as loading control, respectively.

(C) Left: GSH levels in control and *NFE2L2*-KO UACC-62 cells normalized to UACC-62 control cells in the absence of Dox. Of note, GSSG levels were negligibly low. Right: ratio of newly synthesized GSH (GSH m+5) to unlabeled GSH (GSH monoisotopic mass, MIM) in indicated cell lines.

(legend continued on next page)

cells to 60% (Figure S9F). Next, the relevance of KEAP1 was investigated in melanoma cells. *KEAP1* was knocked down in UACC-62 iATF4 cells, resulting in a strong increase of NRF2 levels and its target genes (Figures S9G and S9H). Under these conditions, ATF4 induction no longer impaired cellular viability (Figure S9I). In summary, NRF2 plays an important role in maintaining viability and cellular resilience after ATF4 activation.

DISCUSSION

Here, we describe NRF2 activation as an obligatory consequence of the ISR-mediated ATF4 induction. We identified transcriptional upregulation of the *NFE2L2* gene as well as CHAC1-mediated GSH depletion as two independent mechanisms by which ATF4 exerts its NRF2-stimulatory function.

The IRS is caused by several triggers that lead to the activation of any of the four kinases GCN2, PERK, HRI, and PKR, resulting in ATF4 activation. Intriguingly, most of the kinase triggers have been previously connected to an imbalance in thiol metabolism and oxidative stress. Amino acid depletion, such as glutamine, glutamate, or cysteine starvation, triggers the GCN2 kinase and results in reduced cysteine or GSH supply.² ER stress, the trigger for PERK activity, is closely coupled to a disturbance of the redox balance, which impairs the correct formation of disulfide bonds and, thereby, protein folding.⁴⁵ HRI, originally described to respond primarily to heme deprivation, is in fact activated by multiple triggers including oxidative stress.⁴⁶ The protein kinase PKR is activated by double-stranded RNA, e.g., during viral infection.² Several RNA viruses were reported to impair mitochondrial function or increase NADPH oxidase activity, causing redox imbalance in the host cell.⁴⁷ From an evolutionary perspective, a coupling of the ISR to NRF2 is therefore an efficient means to counteract immediate stress and keep the damage under control. In this context the maintenance of cysteine availability plays a central role, as it is tightly linked to cellular redox balance. Here, we show that ATF4 and NRF2 join forces on multiple levels. As a result of their involvement in *SLC7A11* transcription, ATF4 and NRF2 increase the abundance of the xCT antiporter.^{48,49} Notably, SLC3A2—the binding partner of SLC7A11 in the heterodimeric xCT—is also induced by cysteine deprivation,⁵⁰ suggesting an involvement of ATF4 and/or NRF2. Next to cystine import, ATF4 also increases cysteine *de novo* synthesis by inducing *CTH* and *CBS*, which catalyze the last steps of cysteine synthesis in the trans-sulfuration pathway.^{51,52} In the present study, we further demonstrate CHAC1-driven GSH degradation as another ATF4-dependent means to fuel the xCT transporter, as ATF4 activation in CHAC1-deficient cells had impaired xCT antiporter activity. This reduced xCT activity was likely caused by a combination of reduced glutamate availability

and reduced NRF2 activation occurring in the absence of CHAC1. Of note, the degradation of GSH also generated cysteine-glycine, whose levels were quickly reduced in response to ATF4 activation (Figure S9J), indicating cysteine-glycine dipeptidase activity and further utilization of GSH-derived cysteine.

The observation that ATF4 causes an overall reduction of GSH seems peculiar at first sight, particularly in the light of ATF4-dependent stimulation of *de novo* GSH synthesis that was observed by us and others.⁴¹ However, our data show that GSH levels are strongly affected by both CHAC1-dependent GSH degradation on the one side and *de novo* GSH synthesis on the other side, leading, in the cell lines investigated in this study, to a net GSH decrease. It is, however, likely that several features, e.g., the basal GSH levels of the cells or cell types, the extent of ATF4 induction, and other underlying factors (such as independent NRF2 activators), may affect this balance, thus resulting in different effects on the net GSH levels after ATF4 activation.

Next to the GSH pathway, reduction equivalents such as NADPH play an important role in the intracellular redox balance. Genes of the pentose phosphate pathway such as G6PD and PGD are involved in providing NADPH. Both are not direct ATF4 target genes, and their transcription requires the activity of NRF2. The parallel NRF2-dependent increase of thioredoxin pathway genes further supports the resilience of cells undergoing the ISR and can compensate for the loss of GSH. In line with this, single disruption of the GSH or thioredoxin pathway is well tolerated in mouse models for B cell lymphoma or breast cancer, while a combination of both strongly impairs tumor growth.^{53,54}

Because of the short half-life of both ATF4 and NRF2, the stress response is only transiently active under acute stress. However, chronic stress has a longer-lasting effect on ATF4 and NRF2, e.g., in experimental tumors undergoing adoptive T cell transfer³⁶ and BRAF inhibitor therapy.²⁷ Consequently, the linkage between ATF4 and NRF2 increases cellular resilience and provides the potential to support the survival of tumor cells undergoing therapy or encountering challenging conditions in the tumor microenvironment.

Limitations of the study

When investigating the crosstalk between the effectors of the integrated and oxidative stress response, we found an obligatory ATF4-dependent NRF2 activation, which became the focus of this study and was further characterized. However, we do not exclude a regulation in the reverse direction, and ample data from several research groups including ours indicate indeed an influence of NRF2 on ATF4 activity.^{13–15} Although the NRF2 knockout had no effect on ATF4 target gene expression in our

(D) Left: ratio of exported labeled glutamate (Glu m+5) to unlabeled glutamate (Glu MIM) in the medium of indicated cells after 4 h of previous [¹³C]glutamine labeling. Right: ratio of total extracellular cystine in the medium of Dox-treated (ATF4-induced) versus untreated cells after 4 h.

(E) Protein blot showing CHAC1, ATF4, and NRF2 expression in control (non-targeting gRNA) and *CHAC1*-KO UACC-62 iATF4 cells used for metabolic supernatant analyses after ATF4 induction (100 ng/mL Dox, 3 days). Actin served as loading control.

(F) As in (D), but with control and *CHAC1*-KO cells expressing iATF4, as described in (E).

(G) Schematic overview of the fate of [¹³C]glutamine after its uptake in iATF4 cells. Next to the tricarboxylic acid (TCA) cycle and asparagine synthesis, ATF4 causes a net reduction of GSH, which is used to fuel the xCT transporter to enable cysteine supply. At the same time, ATF4-dependent NRF2 activation enhances GSH synthesis and xCT antiporter activity.

For (C), (D), and (F), significance was calculated by one-way ANOVA with Tukey's multiple comparison test (**p* < 0.05, ***p* < 0.01, ****p* < 0.001). Error bars represent SD.

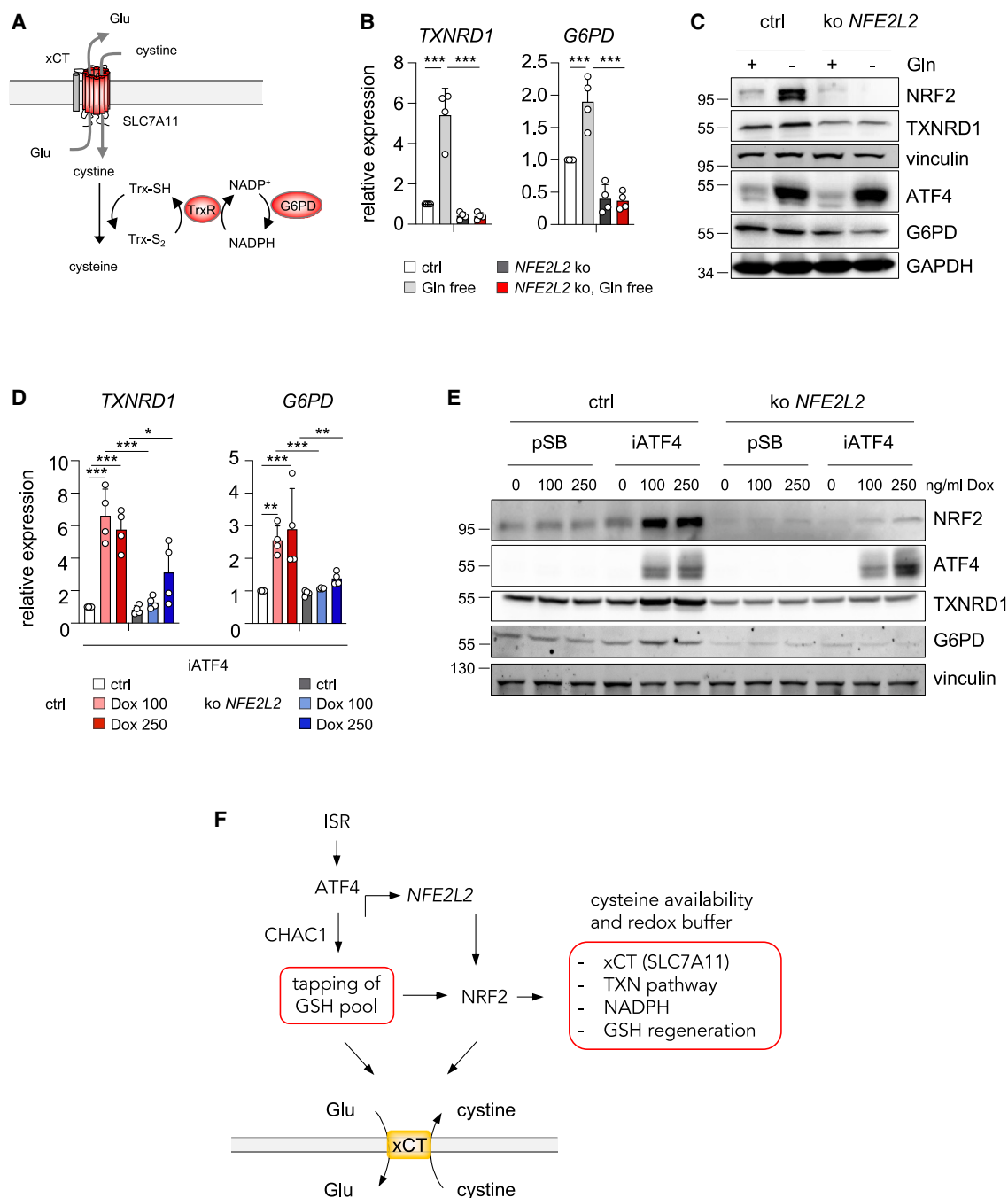


Figure 7. NRF2 maintains thioredoxin and NADPH pathways after ATF4 activation

(A) Overview of cystine import and reduction by the xCT antiporter and thioredoxin/NADPH, respectively, in the absence of glutathione. Trx-SH, reduced thioredoxin; Trx-S₂, oxidized thioredoxin.

(B) Real-time PCR of thioredoxin reductase 1 (*TXNRD1*) and glucose-6-phosphate dehydrogenase (*G6PD*) in control and *NFE2L2*-KO UACC-62 cells. Where indicated, cells were kept in the absence of glutamine for 1 day (n = 4).

(C) Corresponding western blot. GAPDH and vinculin served as loading controls.

(D) Real-time PCR of *TXNRD1* and *G6PD* in control and *NFE2L2*-KO UACC-62 cells with iATF4. Where indicated, cells were kept in the presence of doxycycline (Dox; 100 or 250 ng/mL, 3 days, n = 4).

In (B) and (D), significance was calculated by one-way ANOVA with Dunnett's multiple comparison test (*p < 0.05, **p < 0.01, ***p < 0.001). Error bars represent SD.

(legend continued on next page)

experimental model, we repeatedly observed increased ATF4 protein levels in glutamine- and cystine-starved NRF2-KO cells. It is therefore likely that NRF2 also affects upstream regulators of ATF4 with consequential high relevance, e.g., under conditions of elevated oxidative stress.

Furthermore, we identified CHAC1 as important regulator of NRF2. Although we only observed reasonable CHAC1 protein amounts after stress induction, the CHAC1 knockout already had a major effect on GSH levels in the absence of stress. This implies that low basal CHAC1, probably below detection levels of the commercial antibodies, already regulates basal GSH levels, with possible effects on NRF2 even in the absence of ATF4-inducing stress. The physiological role of CHAC1 under basal conditions requires future studies.

Another gap in knowledge is the molecular basis for CHAC1-mediated NRF2 activation. It is, however, likely that CHAC1-dependent GSH depletion affects the interaction between KEAP1 and NRF2 through altering ROS and GSH levels. KEAP1 contains several cysteine residues that are highly susceptible to oxidative stress and whose oxidative modifications cause conformational changes that impair the binding to NRF2 and result in NRF2 accumulation.⁵⁵ KEAP1 can also be modified by glutathionylation.⁵⁶ A precise analysis of CHAC1-dependent KEAP1 modifications and the resulting altered KEAP1-NRF2 interactions will be essential to further characterize this mode of NRF2 activation.

STAR★METHODS

Detailed methods are provided in the online version of this paper and include the following:

- **KEY RESOURCES TABLE**
- **RESOURCE AVAILABILITY**
 - Lead contact
 - Materials availability
 - Data and code availability
- **EXPERIMENTAL MODEL AND SUBJECT DETAILS**
 - Cell culture
- **METHOD DETAILS**
 - siRNA transfection
 - Stable transfection
 - CRISPR/Cas9 mediated gene knockout
 - MTT assay
 - Protein lysis and western blot
 - Nuclear and cytoplasmic fractionation
 - Mass spectrometry and isotope tracing
 - Immunofluorescence
 - RNA extraction, cDNA synthesis, and RT-qPCR
 - Tietze assay
 - Chromatin immunoprecipitation (ChIP)
- **QUANTIFICATION AND STATISTICAL ANALYSIS**

SUPPLEMENTAL INFORMATION

Supplemental information can be found online at <https://doi.org/10.1016/j.celrep.2023.112724>.

ACKNOWLEDGMENTS

This work was funded by the German Research Foundation (DFG) grant ME1899/6-1. This publication was supported by the Open Access Publication Fund of the University of Wuerzburg.

AUTHOR CONTRIBUTIONS

S.M. designed the study. J.P.F.A. contributed to study design. J.K.C.K., C.J., and A.H. conducted the experiments, with support from T.N.X.d.S. and A.F.d.S. W.S. performed the metabolomics analysis. C.R.G. and L.M. developed methodology and provided ChIP-seq data. S.M. and J.K.C.K. wrote the manuscript. S.M. acquired the funding. All authors discussed the results and revised the manuscript.

DECLARATION OF INTERESTS

The authors declare no competing interests.

INCLUSION AND DIVERSITY

We support inclusive, diverse, and equitable conduct of research.

Received: August 19, 2022

Revised: February 28, 2023

Accepted: June 14, 2023

Published: July 4, 2023

REFERENCES

1. Hanahan, D., and Weinberg, R.A. (2011). Hallmarks of cancer: the next generation. *Cell* 144, 646–674. <https://doi.org/10.1016/j.cell.2011.02.013>.
2. Pakos-Zebrucka, K., Koryga, I., Mnich, K., Lujic, M., Samali, A., and Gorman, A.M. (2016). The integrated stress response. *EMBO Rep.* 17, 1374–1395. <https://doi.org/10.15252/embr.201642195>.
3. Oakes, S.A. (2020). Endoplasmic Reticulum Stress Signaling in Cancer Cells. *Am. J. Pathol.* 190, 934–946. <https://doi.org/10.1016/j.ajpath.2020.01.010>.
4. Kilberg, M.S., Shan, J., and Su, N. (2009). ATF4-dependent transcription mediates signaling of amino acid limitation. *Trends Endocrinol. Metab.* 20, 436–443. <https://doi.org/10.1016/j.tem.2009.05.008>.
5. B'Chir, W., Maurin, A.C., Carraro, V., Averous, J., Jousse, C., Muranishi, Y., Parry, L., Stepien, G., Fafournoux, P., and Bruhat, A. (2013). The eIF2α-phosphatase/ATF4 pathway is essential for stress-induced autophagy gene expression. *Nucleic Acids Res.* 41, 7683–7699. <https://doi.org/10.1093/nar/gkt563>.
6. Cullinan, S.B., Gordan, J.D., Jin, J., Harper, J.W., and Diehl, J.A. (2004). The Keap1-BTB protein is an adaptor that bridges Nrf2 to a Cul3-based E3 ligase: oxidative stress sensing by a Cul3-Keap1 ligase. *Mol. Cell Biol.* 24, 8477–8486. <https://doi.org/10.1128/MCB.24.19.8477-8486.2004>.
7. Kobayashi, A., Kang, M.I., Okawa, H., Ohtsui, M., Zenke, Y., Chiba, T., Igarashi, K., and Yamamoto, M. (2004). Oxidative stress sensor Keap1 functions as an adaptor for Cul3-based E3 ligase to regulate proteasomal

(E) Corresponding western blot using vinculin as loading control.

(F) Overview of the mode of interaction between ATF4 and NRF2. After activation through the integrated stress response (ISR), ATF4 triggers NRF2 directly via transcription and indirectly via CHAC1-mediated GSH degradation. Glutamate, derived from this degradation, contributes to xCT activity, along with ATF4- and NRF2-dependent transcriptional upregulation of the xCT component SLC7A11. NRF2 furthermore increases thioredoxin (TXN) pathway components and NADPH regeneration to meet antioxidant requirements under GSH depletion.

- degradation of Nrf2. *Mol. Cell Biol.* 24, 7130–7139. <https://doi.org/10.1128/MCB.24.16.7130-7139.2004>.
8. Zhang, D.D., and Hannink, M. (2003). Distinct cysteine residues in Keap1 are required for Keap1-dependent ubiquitination of Nrf2 and for stabilization of Nrf2 by chemopreventive agents and oxidative stress. *Mol. Cell Biol.* 23, 8137–8151. <https://doi.org/10.1128/mcb.23.22.8137-8151.2003>.
9. Hirotsu, Y., Katsuoka, F., Funayama, R., Nagashima, T., Nishida, Y., Nakayama, K., Engel, J.D., and Yamamoto, M. (2012). Nrf2-MafG heterodimers contribute globally to antioxidant and metabolic networks. *Nucleic Acids Res.* 40, 10228–10239. <https://doi.org/10.1093/nar/gks827>.
10. Katsuoka, F., Motohashi, H., Ishii, T., Aburatani, H., Engel, J.D., and Yamamoto, M. (2005). Genetic evidence that small maf proteins are essential for the activation of antioxidant response element-dependent genes. *Mol. Cell Biol.* 25, 8044–8051. <https://doi.org/10.1128/MCB.25.18.8044-8051.2005>.
11. Malhotra, J.D., and Kaufman, R.J. (2007). Endoplasmic reticulum stress and oxidative stress: a vicious cycle or a double-edged sword? *Antioxidants Redox Signal.* 9, 2277–2293. <https://doi.org/10.1089/ars.2007.1782>.
12. Cullinan, S.B., Zhang, D., Hannink, M., Arvisais, E., Kaufman, R.J., and Diehl, J.A. (2003). Nrf2 is a direct PERK substrate and effector of PERK-dependent cell survival. *Mol. Cell Biol.* 23, 7198–7209. <https://doi.org/10.1128/mcb.23.20.7198-7209.2003>.
13. Gwinn, D.M., Lee, A.G., Briones-Martin-Del-Campo, M., Conn, C.S., Simpson, D.R., Scott, A.I., Le, A., Cowan, T.M., Ruggero, D., and Sweet-Cordero, E.A. (2018). Oncogenic KRAS Regulates Amino Acid Homeostasis and Asparagine Biosynthesis via ATF4 and Alters Sensitivity to L-Asparaginase. *Cancer Cell* 33, 91–107.e6. <https://doi.org/10.1016/j.ccell.2017.12.003>.
14. DeNicola, G.M., Chen, P.H., Mullarky, E., Sudderth, J.A., Hu, Z., Wu, D., Tang, H., Xie, Y., Asara, J.M., Huffman, K.E., et al. (2015). NRF2 regulates serine biosynthesis in non-small cell lung cancer. *Nat. Genet.* 47, 1475–1481. <https://doi.org/10.1038/ng.3421>.
15. Jessen, C., Kreß, J.K.C., Baluapuri, A., Hufnagel, A., Schmitz, W., Kneitz, S., Roth, S., Marquardt, A., Appenzeller, S., Ade, C.P., et al. (2020). The transcription factor NRF2 enhances melanoma malignancy by blocking differentiation and inducing COX2 expression. *Oncogene* 39, 6841–6855. <https://doi.org/10.1038/s41388-020-01477-8>.
16. Altea-Manzano, P., Cuadros, A.M., Broadfield, L.A., and Fendt, S.M. (2020). Nutrient metabolism and cancer in the in vivo context: a metabolic game of give and take. *EMBO Rep.* 21, e50635. <https://doi.org/10.15252/embr.202050635>.
17. Ubellacker, J.M., Tasdogan, A., Ramesh, V., Shen, B., Mitchell, E.C., Martin-Sandoval, M.S., Gu, Z., McCormick, M.L., Durham, A.B., Spitz, D.R., et al. (2020). Lymph protects metastasizing melanoma cells from ferroptosis. *Nature* 585, 113–118. <https://doi.org/10.1038/s41586-020-2623-z>.
18. Piskounova, E., Agathocleous, M., Murphy, M.M., Hu, Z., Huddleston, S.E., Zhao, Z., Leitch, A.M., Johnson, T.M., DeBerardinis, R.J., and Morrison, S.J. (2015). Oxidative stress inhibits distant metastasis by human melanoma cells. *Nature* 527, 186–191. <https://doi.org/10.1038/nature15726>.
19. Riesenberger, S., Groetchen, A., Siddaway, R., Bald, T., Reinhardt, J., Smorra, D., Kohlmeyer, J., Renn, M., Phung, B., Aymans, P., et al. (2015). MITF and c-Jun antagonism interconnects melanoma dedifferentiation with pro-inflammatory cytokine responsiveness and myeloid cell recruitment. *Nat. Commun.* 6, 8755. <https://doi.org/10.1038/ncomms9755>.
20. Landsberg, J., Kohlmeyer, J., Renn, M., Bald, T., Rogava, M., Cron, M., Fatho, M., Lennerz, V., Wölfel, T., Hölzel, M., and Tüting, T. (2012). Melanomas resist T-cell therapy through inflammation-induced reversible dedifferentiation. *Nature* 490, 412–416. <https://doi.org/10.1038/nature11538>.
21. Falletta, P., Sanchez-Del-Campo, L., Chauhan, J., Effer, M., Kenyon, A., Kershaw, C.J., Siddaway, R., Lisle, R., Freter, R., Daniels, M.J., et al. (2017). Translation reprogramming is an evolutionarily conserved driver of phenotypic plasticity and therapeutic resistance in melanoma. *Genes Dev.* 31, 18–33. <https://doi.org/10.1101/gad.290940.116>.
22. Koppula, P., Zhang, Y., Shi, J., Li, W., and Gan, B. (2017). The glutamate/cystine antiporter SLC7A11/xCT enhances cancer cell dependency on glucose by exporting glutamate. *J. Biol. Chem.* 292, 14240–14249. <https://doi.org/10.1074/jbc.M117.798405>.
23. Itoh, K., Wakabayashi, N., Katoh, Y., Ishii, T., Igarashi, K., Engel, J.D., and Yamamoto, M. (1999). Keap1 represses nuclear activation of antioxidant responsive elements by Nrf2 through binding to the amino-terminal Neh2 domain. *Genes Dev.* 13, 76–86. <https://doi.org/10.1101/gad.13.1.76>.
24. Jin, H.O., Seo, S.K., Woo, S.H., Kim, E.S., Lee, H.C., Yoo, D.H., An, S., Choe, T.B., Lee, S.J., Hong, S.I., et al. (2009). Activating transcription factor 4 and CCAAT/enhancer-binding protein-beta negatively regulate the mammalian target of rapamycin via Redd1 expression in response to oxidative and endoplasmic reticulum stress. *Free Radic. Biol. Med.* 46, 1158–1167. <https://doi.org/10.1016/j.freeradbiomed.2009.01.015>.
25. Khamari, R., Trinh, A., Gabert, P.E., Corazao-Rozas, P., Riveros-Cruz, S., Balayssac, S., Malet-Martino, M., Dekioui, S., Joncquel Chevalier Curt, M., Maboudou, P., et al. (2018). Glucose metabolism and NRF2 coordinate the antioxidant response in melanoma resistant to MAPK inhibitors. *Cell Death Dis.* 9, 325. <https://doi.org/10.1038/s41419-018-0340-4>.
26. Nagasawa, I., Koido, M., Tani, Y., Tsukahara, S., Kunimasa, K., and Tomida, A. (2020). Disrupting ATF4 Expression Mechanisms Provides an Effective Strategy for BRAF-Targeted Melanoma Therapy. *iScience* 23, 101028. <https://doi.org/10.1016/j.isci.2020.101028>.
27. Yang, C., Tian, C., Hoffman, T.E., Jacobsen, N.K., and Spencer, S.L. (2021). Melanoma subpopulations that rapidly escape MAPK pathway inhibition incur DNA damage and rely on stress signalling. *Nat. Commun.* 12, 1747. <https://doi.org/10.1038/s41467-021-21549-x>.
28. Rambow, F., Rogiers, A., Marin-Bejar, O., Aibar, S., Femel, J., Dewaele, M., Karras, P., Brown, D., Chang, Y.H., Debicq-Rychter, M., et al. (2018). Toward Minimal Residual Disease-Directed Therapy in Melanoma. *Cell* 174, 843–855.e19. <https://doi.org/10.1016/j.cell.2018.06.025>.
29. Costa-Mattioli, M., Gobert, D., Stern, E., Gamache, K., Colina, R., Cuellar, C., Sossin, W., Kaufman, R., Pelletier, J., Rosenblum, K., et al. (2007). eIF2alpha phosphorylation bidirectionally regulates the switch from short- to long-term synaptic plasticity and memory. *Cell* 129, 195–206. <https://doi.org/10.1016/j.cell.2007.01.050>.
30. Hu, C., Egger, A.L., Mesecar, A.D., and van Breemen, R.B. (2011). Modification of keap1 cysteine residues by sulforaphane. *Chem. Res. Toxicol.* 24, 515–521. <https://doi.org/10.1021/tx100389r>.
31. Pan, D., Yang, W., Zeng, Y., Qin, H., Xu, Y., Gui, Y., Fan, X., Tian, G., Wu, Y., Sun, H., et al. (2022). AKR1C3 regulated by NRF2/MAFG complex promotes proliferation via stabilizing PARP1 in hepatocellular carcinoma. *Oncogene* 41, 3846–3858. <https://doi.org/10.1038/s41388-022-02379-7>.
32. MacLeod, A.K., Acosta-Jimenez, L., Coates, P.J., McMahon, M., Carey, F.A., Honda, T., Henderson, C.J., and Wolf, C.R. (2016). Aldo-keto reductases are biomarkers of NRF2 activity and are co-ordinately overexpressed in non-small cell lung cancer. *Br. J. Cancer* 115, 1530–1539. <https://doi.org/10.1038/bjc.2016.363>.
33. Hawkes, H.J.K., Karlenius, T.C., and Tonissen, K.F. (2014). Regulation of the human thioredoxin gene promoter and its key substrates: a study of functional and putative regulatory elements. *Biochim. Biophys. Acta* 1840, 303–314. <https://doi.org/10.1016/j.bbagen.2013.09.013>.
34. Dempster, J.M., Boyle, I., Vazquez, F., Root, D.E., Boehm, J.S., Hahn, W.C., Tsherniak, A., and McFarland, J.M. (2021). Chronos: a cell population dynamics model of CRISPR experiments that improves inference of gene fitness effects. *Genome Biol.* 22, 343. <https://doi.org/10.1186/s13059-021-02540-7>.
35. Sarcinelli, C., Dragic, H., Piecyk, M., Barbet, V., Duret, C., Barthelais, A., Ferraro-Peyret, C., Fauvre, J., Renno, T., Chaveroux, C., and Manié, S.N. (2020). ATF4-Dependent NRF2 Transcriptional Regulation Promotes

- Antioxidant Protection during Endoplasmic Reticulum Stress. *Cancers* 12, 569. <https://doi.org/10.3390/cancers12030569>.
36. Vivas-Garcia, Y., Falletta, P., Liebing, J., Louphrasitthiphol, P., Feng, Y., Chauhan, J., Scott, D.A., Glodde, N., Chocarro-Calvo, A., Bonham, S., et al. (2020). Lineage-Restricted Regulation of SCD and Fatty Acid Saturation by MITF Controls Melanoma Phenotypic Plasticity. *Mol. Cell*. 77, 120–137.e129. <https://doi.org/10.1016/j.molcel.2019.10.014>.
37. Fornes, O., Castro-Mondragon, J.A., Khan, A., van der Lee, R., Zhang, X., Richmond, P.A., Modi, B.P., Correard, S., Gheorghe, M., Baranašić, D., et al. (2020). JASPAR 2020: update of the open-access database of transcription factor binding profiles. *Nucleic Acids Res.* 48, D87–D92. <https://doi.org/10.1093/nar/gkz1001>.
38. Schmidlin, C.J., Shakya, A., Dodson, M., Chapman, E., and Zhang, D.D. (2021). The intricacies of NRF2 regulation in cancer. *Semin. Cancer Biol.* 76, 110–119. <https://doi.org/10.1016/j.semcancer.2021.05.016>.
39. Tietze, F. (1969). Enzymic method for quantitative determination of nanogram amounts of total and oxidized glutathione: applications to mammalian blood and other tissues. *Anal. Biochem.* 27, 502–522. [https://doi.org/10.1016/0003-2697\(69\)90064-5](https://doi.org/10.1016/0003-2697(69)90064-5).
40. Lee, H.R., Cho, J.M., Shin, D.H., Yong, C.S., Choi, H.G., Wakabayashi, N., and Kwak, M.K. (2008). Adaptive response to GSH depletion and resistance to L-buthionine-(S,R)-sulfoximine: involvement of Nrf2 activation. *Mol. Cell. Biochem.* 318, 23–31. <https://doi.org/10.1007/s11010-008-9853-y>.
41. Torrence, M.E., MacArthur, M.R., Hosios, A.M., Valvezan, A.J., Asara, J.M., Mitchell, J.R., and Manning, B.D. (2021). The mTORC1-mediated activation of ATF4 promotes protein and glutathione synthesis downstream of growth signals. *Elife* 10, e63326. <https://doi.org/10.7554/eLife.63326>.
42. Ghandi, M., Huang, F.W., Jané-Valbuena, J., Kryukov, G.V., Lo, C.C., McDonald, E.R., 3rd, Barretina, J., Gelfand, E.T., Bielski, C.M., Li, H., et al. (2019). Next-generation characterization of the Cancer Cell Line Encyclopedia. *Nature* 569, 503–508. <https://doi.org/10.1038/s41586-019-1186-3>.
43. Mandal, P.K., Seiler, A., Perisic, T., Kölle, P., Banjac Canak, A., Förster, H., Weiss, N., Kremmer, E., Lieberman, M.W., Bannai, S., et al. (2010). System x(c)- and thioredoxin reductase 1 cooperatively rescue glutathione deficiency. *J. Biol. Chem.* 285, 22244–22253. <https://doi.org/10.1074/jbc.M110.121327>.
44. Singh, A., Misra, V., Thimmulappa, R.K., Lee, H., Ames, S., Hoque, M.O., Herman, J.G., Baylin, S.B., Sidransky, D., Gabrielson, E., et al. (2006). Dysfunctional KEAP1-NRF2 interaction in non-small-cell lung cancer. *PLoS Med.* 3, e420. <https://doi.org/10.1371/journal.pmed.0030420>.
45. Zhang, Z., Zhang, L., Zhou, L., Lei, Y., Zhang, Y., and Huang, C. (2019). Redox signaling and unfolded protein response coordinate cell fate decisions under ER stress. *Redox Biol.* 25, 101047. <https://doi.org/10.1016/j.redox.2018.11.005>.
46. Girardin, S.E., Cuziol, C., Philpott, D.J., and Arnoult, D. (2021). The eIF2 α kinase HRI in innate immunity, proteostasis, and mitochondrial stress. *FEBS J.* 288, 3094–3107. <https://doi.org/10.1111/febs.15553>.
47. Sander, W.J., Fourie, C., Sabiu, S., O'Neill, F.H., Pohl, C.H., and O'Neill, H.G. (2022). Reactive oxygen species as potential antiviral targets. *Rev. Med. Virol.* 32, e2240. <https://doi.org/10.1002/rmv.2240>.
48. Chen, D., Fan, Z., Rauh, M., Buchfelder, M., Eyupoglu, I.Y., and Savaskan, N. (2017). ATF4 promotes angiogenesis and neuronal cell death and confers ferroptosis in a xCT-dependent manner. *Oncogene* 36, 5593–5608. <https://doi.org/10.1038/onc.2017.146>.
49. Sasaki, H., Sato, H., Kuriyama-Matsumura, K., Sato, K., Maebara, K., Wang, H., Tamba, M., Itoh, K., Yamamoto, M., and Bannai, S. (2002). Electrophile response element-mediated induction of the cystine/glutamate exchange transporter gene expression. *J. Biol. Chem.* 277, 44765–44771. <https://doi.org/10.1074/jbc.M208704200>.
50. Lee, J.I., Dominy, J.E., Jr., Sikilidis, A.K., Hirschberger, L.L., Wang, W., and Stipanuk, M.H. (2008). HepG2/C3A cells respond to cysteine deprivation by induction of the amino acid deprivation/integrated stress response pathway. *Physiol. Genom.* 33, 218–229. <https://doi.org/10.1152/physiol-genomics.00263.2007>.
51. Dickhout, J.G., Carlisle, R.E., Jerome, D.E., Mohammed-Ali, Z., Jiang, H., Yang, G., Mani, S., Garg, S.K., Banerjee, R., Kaufman, R.J., et al. (2012). Integrated stress response modulates cellular redox state via induction of cystathionine gamma-lyase: cross-talk between integrated stress response and thiol metabolism. *J. Biol. Chem.* 287, 7603–7614. <https://doi.org/10.1074/jbc.M111.304576>.
52. Zhu, J., Berisa, M., Schwörer, S., Qin, W., Cross, J.R., and Thompson, C.B. (2019). Transsulfuration Activity Can Support Cell Growth upon Extracellular Cysteine Limitation. *Cell Metabol.* 30, 865–876.e5. <https://doi.org/10.1016/j.cmet.2019.09.009>.
53. Mandal, P.K., Schneider, M., Kölle, P., Kuhlencordt, P., Förster, H., Beck, H., Bornkamm, G.W., and Conrad, M. (2010). Loss of thioredoxin reductase 1 renders tumors highly susceptible to pharmacologic glutathione deprivation. *Cancer Res.* 70, 9505–9514. <https://doi.org/10.1158/0008-5472.CAN-10-1509>.
54. Harris, I.S., Treloar, A.E., Inoue, S., Sasaki, M., Gorrini, C., Lee, K.C., Yung, K.Y., Brenner, D., Knobbe-Thomsen, C.B., Cox, M.A., et al. (2015). Glutathione and thioredoxin antioxidant pathways synergize to drive cancer initiation and progression. *Cancer Cell* 27, 211–222. <https://doi.org/10.1016/j.ccell.2014.11.019>.
55. Pillai, R., Hayashi, M., Zavitsanou, A.M., and Papagiannakopoulos, T. (2022). NRF2: KEAPing Tumors Protected. *Cancer Discov.* 12, 625–643. <https://doi.org/10.1158/2159-8290.CD-21-0922>.
56. Carvalho, A.N., Marques, C., Guedes, R.C., Castro-Caldas, M., Rodrigues, E., van Horssen, J., and Gama, M.J. (2016). S-Glutathionylation of Keap1: a new role for glutathione S-transferase pi in neuronal protection. *FEBS Lett.* 590, 1455–1466. <https://doi.org/10.1002/1873-3468.12177>.
57. Mátés, L., Chuah, M.K.L., Belay, E., Jerchow, B., Manoj, N., Acosta-Sanchez, A., Grzela, D.P., Schmitt, A., Becker, K., Matrai, J., et al. (2009). Molecular evolution of a novel hyperactive Sleeping Beauty transposase enables robust stable gene transfer in vertebrates. *Nat. Genet.* 41, 753–761. <https://doi.org/10.1038/ng.343>.
58. Chu, V.T., Weber, T., Wefers, B., Wurst, W., Sander, S., Rajewsky, K., and Kühn, R. (2015). Increasing the efficiency of homology-directed repair for CRISPR-Cas9-induced precise gene editing in mammalian cells. *Nat. Biotechnol.* 33, 543–548. <https://doi.org/10.1038/nbt.3198>.
59. Kreß, J.K.C., Jessen, C., Marquardt, A., Hufnagel, A., and Meierjohann, S. (2021). NRF2 Enables EGFR Signaling in Melanoma Cells. *Int. J. Mol. Sci.* 22, 3803. <https://doi.org/10.3390/ijms22083803>.
60. Louphrasitthiphol, P., Siddaway, R., Loffreda, A., Pogenberg, V., Friedrichsen, H., Schepsky, A., Zeng, Z., Lu, M., Strub, T., Freter, R., et al. (2020). Tuning Transcription Factor Availability through Acetylation-Mediated Genomic Redistribution. *Mol. Cell.* 79, 472–487.e10. <https://doi.org/10.1016/j.molcel.2020.05.025>.

STAR★METHODS

KEY RESOURCES TABLE

REAGENT or RESOURCE	SOURCE	IDENTIFIER
Antibodies		
Anti-CHAC1 antibody	Sigma-Aldrich	Cat#SAB2700669
Anti-CHAC1 antibody	Sigma-Aldrich	Cat#AV42623; RRID:AB_1846608
Anti- β -Actin Antibody (C4)	Santa Cruz Biotechnology	Cat#sc-47778; RRID:AB_626632
Asparagine synthetase (G-10)	Santa Cruz Biotechnology	Cat#sc-365809; RRID:AB_10843357
ATF-4 (D4B8) Rabbit mAb	Cell Signaling Technology	Cat#11815; RRID: AB_2616025
F(ab') ₂ -Goat anti-Mouse IgG (H + L) Cross-Adsorbed Secondary Antibody, Alexa Fluor™ 488	Invitrogen	Cat#A-11017; RRID:AB_2534084
G6PD (G-12)	Santa Cruz Biotechnology	Cat#sc-373886; RRID:AB_10918100
GAPDH (G-9)	Santa Cruz Biotechnology	Cat#sc-365062; RRID:AB_10847862
Goat Anti-Mouse IgG (H + L) Secondary Antibody, HRP	Thermo Fisher Scientific	Cat# 31444; RRID:AB_228307
Goat Anti-Rabbit IgG (H L)-HRP Conjugate	Bio-Rad	Cat#170-6515; RRID:AB_11125142
Goat anti-Rabbit IgG (H + L) Cross-Adsorbed ReadyProbes Secondary Antibody, Alexa Fluor™ 594	Thermo Fisher Scientific	Cat#11037; RRID:AB_2556545
KEAP1	Cell Signaling Technology	Cat#4678; RRID: AB_10548196
Lamin B1 (B10)	Santa Cruz Biotechnology	Cat#sc-374015; RRID:AB_10947408
Mouse Anti-Vinculin monoclonal antibody	Sigma-Aldrich	Cat# V9131; RRID:AB_477629
Nrf2 antibody [EP1808Y]	abcam	Cat#ab62352; RRID: AB_944418
TRXR1 (D1T3D) Rabbit mAb	Cell Signaling Technology	Cat#15140; RRID: AB_2798725
xCT/SLC7A11 (D2M7A) Rabbit antibody	Cell Signaling Technology	Cat#12691; RRID: AB_2687474
Chemicals, peptides, and recombinant proteins		
3-(4,5-Dimethylthiazol-2-yl)-2,5-diphenyltetrazoliumbromide (MTT reagent)	Sigma-Aldrich	Cat#M2128; CAS: 298-93-1
5-Sulfosalicylic acid hydrate (SSA)	Sigma-Aldrich	Cat#390275; CAS: 5965-83-3
5,5-Dithiobis(2-nitrobenzoic acid) (DTNB)	Sigma-Aldrich	Cat#D8130; CAS: 69-78-3
Acrylamide	Roth	Cat#T802.1; CAS: 79-06-1
Auranofin	Sigma-Aldrich	Cat#6733; CAS: 34031-32-8
BSA	Serva	Cat#11930; CAS: 9048-46-8
BSO	Sigma-Aldrich	Cat#19176; CAS: 5072-26-4
Bsp119I (BstBI)	Thermo Fisher Scientific	Cat#ER0121
BTdCPU	Calbiochem	Cat#324892; CAS: 1257423-87-2
Cycloheximide	AppliChem	Cat#A0879; CAS 66-81-9
Cystine	Sigma-Aldrich	Cat#C8755; CAS: 56-89-3
DMEM	PAN	Cat#P04-03550
DMEM (without L-Glutamine, L-Methionine and L-Cystine)	Thermo Fisher Scientific	Cat#21013-024
Doxycycline	Calbiochem	Cat#324385; CAS: 24390-14-5
DpnI	Thermo Fisher Scientific	Cat#ER170
Erastin	Cayman	Cat#61-90-5; CAS: 61-90-5
FAST AP	Thermo Fisher Scientific	Cat#EF0654
Fetal bovine serum	Sigma-Aldrich	Cat#F7524

(Continued on next page)

Continued

REAGENT or RESOURCE	SOURCE	IDENTIFIER
GlutaMax	Thermo Fisher Scientific	Cat#35050-061
Glutathione reductase	Sigma-Aldrich	Cat#G3664; CAS: 9001-48-3
Hoechst 33342	Invitrogen	Cat#H3570; CAS: 23491-52-3
Hygromycin B	Capricorn Scientific	Cat#HYG-H; CAS: 31282-04-9
L-Glutathione reduced	Sigma-Aldrich	Cat#G4251; CAS: 70-18-8
Methionine	Sigma-Aldrich	Cat#M5308; CAS: 63-68-3
Nicotinamide adenine dinucleotide phosphate (NADPH)	Biomol	Cat# 16156; CAS: 2646-71-1
Nonfat dried milk powder	AppliChem	Cat#A0830
OptiMEM	Invitrogen	Cat#11058-021
Penicillin/Streptomycin	Sigma-Aldrich	Cat#P0781
Protease inhibitor (PIC)	Sigma-Aldrich	Cat#P8340
Primer “random”	Roche	Cat# 11034731001
Puromycin	Calbiochem	Cat#P9620; CAS: 58-58-2
Q5 High-Fidelity DNA Polymerase	NEB	Cat#M0491S
Salubrinal	Sigma-Aldrich	Cat#SML0951; CAS: 405060-95-9
Sulforaphane	LKT lab	Cat#S8047; CAS: 4478-93-7
SYBR green	Invitrogen	Cat#S7563; CAS: 163795-75-3
T4 DNA ligase	Invitrogen	Cat# 15224017
Trypsin 0.5%/EDTA 0.2% in PBS	PAN	Cat#P10-024100
Tunicamycin	Sigma-Aldrich	Cat#654380; CAS: 11089-65-9
Critical commercial assays		
cDNA synthesis Kit	Thermo Fisher Scientific	Cat#K1622
Fugene HD transfection reagent	Promega	Cat# E2311
QIAamp DNA Mini Kit	Qiagen	Cat#61304
SuperSignal™ West Pico PLUS Chemiluminescent Substrate	Thermo Fisher Scientific	Cat#34577
TRIzol reagent	Invitrogen	Cat#15596018
XtremeGene siRNA transfection reagent	Roche	Cat# 04 476 093 001
Deposited data		
Original immunoblots	Mendeley Data Repository	https://doi.org/10.17632/4c28f788v4.1
Experimental models: Cell lines		
UACC-62	NCI/NIH	N/A
M14	NCI/NIH	N/A
H23	ATCC	N/A
A549	ATCC	N/A
MDA-MB-468	ATCC	N/A
Oligonucleotides		
Oligonucleotides for cloning, ChIP, siRNA transfection or for RT-PCR, see Table S1	Sigma-Aldrich	N/A
Recombinant DNA		
pCMV (CAT)T7-SB100X	(Mátés, L., et al.) ⁵⁷	Addgene, Cat#34879
pU6-(BbsI)CBh-Cas9-T2A-mCherry	(Chu, V.T., et al.) ⁵⁸	Addgene, Cat#64324
Software and algorithms		
Carestream Molecular Imaging	Carestream	N/A
CFX Manager Software	Bio-Rad	N/A
Fiji	ImageJ	N/A
Fusion FX Software	Vilber	N/A

(Continued on next page)

Continued

REAGENT or RESOURCE	SOURCE	IDENTIFIER
GraphPad Prism9 software	GraphPad Software	N/A
Leica application suite	Leica	N/A
TraceFinder™ V 3.3	Thermo Fisher Scientific	N/A

RESOURCE AVAILABILITY

Lead contact

Further information and requests for resources and reagents should be directed to and will be fulfilled by the lead contact, Svenja Meierjohann (svenja.meierjohann@uni-wuerzburg.de).

Materials availability

Plasmids and cell lines generated in this study are available from the [lead contact](#) on request.

Data and code availability

- Microarray and RNA seq data reanalysed in this study were previously deposited in the Gene Expression Omnibus (GEO) under the accession numbers GEO: GSE99925, GEO: GSE40213, GEO: GSE86806 and GEO: GSE158605. Original immunoblots have been deposited to Mendeley Data Repository and are available at <https://doi.org/10.17632/4c28f788v4.1>.
- This paper does not report any original code.
- Any information required to reanalyze the data reported in this paper is available from the [lead contact](#) upon request.

EXPERIMENTAL MODEL AND SUBJECT DETAILS

Cell culture

UACC-62 and M14 cells were obtained from NCI/NIH (DCTD Tumor Repository, National Cancer Institute at Frederick, Frederick, MD, USA). H23 and A549 lung adenocarcinoma and MDA-MB-468 breast cancer cells were obtained from the American Type Culture Collection (ATCC). All cells have been authenticated and are regularly tested for contaminations. Cultivation was done in DMEM with 10% FCS (PAN biotech, Aidenbach, Germany) and 1% penicillin/streptomycin (Sigma-Aldrich, St. Louis, MO, USA) at 37°C and 5% CO₂. Where indicated, doxycycline, salubrinal, BSO, auranofin or tunicamycin (Sigma-Aldrich, St. Louis, MO, USA), sulforaphane (LKT Laboratories, St Paul, MN, USA), cycloheximide (AppliChem, Darmstadt, Germany), BTdCPU (Calbiochem/Merck, Darmstadt, Germany) or erastin (Cayman Chemical, Ann Arbor, MI, USA) was added. For cystine-free or glutamine-free medium, DMEM lacking glutamine, methionine and cystine (Thermo Fisher Scientific, Waltham, USA) containing 10% FCS and 1% penicillin/streptomycin was used and 1x GlutaMax (Thermo Fisher Scientific, Waltham, USA), 200 μM methionine (Sigma-Aldrich, St Louis, USA) and 200 μM cystine (Sigma-Aldrich, St Louis, USA) were omitted or added, depending on the required medium composition. As control, all supplements were added to obtain fully reconstituted medium.

METHOD DETAILS

siRNA transfection

Non-targeting siRNA (Sigma-Aldrich, St Louis, USA) or siRNA directed against human ATF4 (Horizon Discovery Bioscience, Cambridge, UK) or human KEAP1 (Horizon Discovery Bioscience, Cambridge, UK) was delivered to the cells using XtremeGene siRNA transfection reagent (Roche, Basel, Switzerland). Transfection was performed according to the manufacturer's protocol. siRNA identifier are shown in [Table S1](#).

Stable transfection

For the doxycycline-inducible expression of ATF4, the pSB-ET-iE-ATF4 construct (shortly pSB-ATF4) was used.¹⁵ To generate the CHAC1 overexpression construct, human CHAC1 was amplified via PCR and was cloned into the transposase vector pSB-ET-iE (see cloning primers in [Table S1](#)). Integration occurred after co-transfection with the sleeping beauty transposase vector pCMV-(CAT)T7-SB100. To generate stable melanoma and NSCLC cells, the respective expression construct was transfected with Fugene HD transfection reagent (Promega, Fitchburg, Massachusetts, USA) according to the manufacturer's protocol. Positive cells were selected with 2 μg/mL puromycin (Calbiochem/Merck, Darmstadt, Germany).

CRISPR/Cas9 mediated gene knockout

For CRISPR/Cas9 mediated gene knockout in human melanoma cells, gRNA expression constructs were generated by cloning the respective gRNA template into the vector pU6-(BbsI)CBh-Cas9-T2A-mCherry (Addgene #64324). Cloning primers for gRNA targeting *NFE2L2* and *ATF4* were described previously,¹⁵ while those targeting *CHAC1* are described in Table S1. Non-targeting gRNA constructs served as controls. Human melanoma cell lines were transfected with gRNA constructs by using Eugene HD transfection reagent (Promega, Fitchburg, USA). Cells were then selected using 350 µg/mL hygromycin (Sigma-Aldrich, St Louis, USA) and single clones were picked and reseeded. gDNA was isolated from single cell clones (QIAamp DNA Mini Kit, Qiagen).

MTT assay

Cells were seeded in triplicates in a 96-well plate at equal numbers. After indicated treatment, 5 mg/mL MTT (3-(4,5-dimethylthiazol-2-yl)-2,5-diphenyltetrazolium bromide) (Sigma-Aldrich, St Louis, USA) was added at a ratio of 1:5 to the cells for 2 h. Afterward, cells were lysed with 150 µL DMSO for 20 min. Analysis of the developed formazan accumulation was performed in a microplate reader (FLUOstar Omega, BMG Labtech, Ortenberg, Germany) at 590 nm with a reference filter of 620 nm.

Protein lysis and western blot

Cells were lysed in RIPA lysis buffer (50 mM Tris pH 8.0; 50 mM NaCl; 1% Nonidet-P40; 0.5% deoxycholate, 0.1% SDS; 10 µg/mL aprotinin; 10 µg/mL leupeptin; 200 µM Na₃VO₄; 1 mM PMSF; and 100 mM NaF). Shortly after, 40 µg of protein was separated by 10–14% polyacrylamide SDS-PAGE. Proteins were transferred onto Amersham nitrocellulose membranes (GE Healthcare, Chicago, IL, USA) and were blocked with 5% BSA (Serva, Heidelberg, Germany) in TBS with 0.1% Tween 20. Incubation with the primary antibodies took place at 4°C overnight. The following antibodies were used in this study: NRF2 ([EP1808Y], ab62352) antibody was purchased from Abcam, Cambridge, UK. Antibodies directed against ATF4 (#11815), TXNRD1 (#15140), and KEAP1 (#4678) were from Cell Signaling Technology, Danvers, USA. Antibodies against G6PD (sc-373886), ASNS (sc-365809), beta-actin (sc-47778), Lamin B1 (sc-374015) and GAPDH (sc-365062) were purchased from Santa Cruz Biotechnology (Dallas, TX, USA). Anti-vinculin (V9131) and anti-CHAC1 (#SAB2700669 or #AV42623) were purchased from Sigma-Aldrich (St. Louis, MO, USA). Antibody directed against SLC7A11 (#PA1-16893) was from Thermo Fisher Scientific (Waltham, MA, USA). For protein detection, membranes were incubated with secondary antibodies: anti-mouse (31444, Thermo Scientific, Waltham, MA, USA) or anti-rabbit (170–6515, Bio-Rad, CA, USA), were coupled to horseradish peroxidase and visualized with the ECL detection kit (Thermo Fisher Scientific, Waltham, MA, USA) or with the Alexa Fluor 488 anti-mouse antibody (A11017) (Invitrogen, Carlsbad, CA, USA) and a Fusion SL imaging system (Vilber Lourmat, Eberhardzell, Germany). In each western blot, the molecular weight (kDa) of the most adjacent molecular weight marker is shown.

Nuclear and cytoplasmic fractionation

Cells were resuspended in cold PBS and freshly added inhibitors (dithiothreitol (1:1000), phenylmethylsulfonylfluoride (1:100), protease inhibitor cocktail (Sigma-Aldrich, St. Louis, USA, 1:1000), β-glycerophosphate (1:100)). After centrifugation, the supernatant was discarded and cell pellets were lysed in PBS and 0.1% NP-40 with freshly prepared inhibitors. The resulting lysate contained the cytosolic fraction and was collected for further analysis. The lysis step was repeated to improve the purity of the nuclear fraction. After centrifugation, the nuclear pellet was lysed in nuclei lysis buffer (20 mM HEPES pH 7.4, 400 mM NaCl, 1.5 mM MgCl₂, 0.1 mM EDTA, 15% glycerol) with freshly added inhibitors. Following 15 min of incubation on ice, samples were sonicated in a Bioruptor (Diagenode, Denville, USA). To pelletize the nuclear cell debris, samples were centrifuged at 4°C. Supernatants containing the nuclear lysate were transferred into new tubes and were used for western blot analysis.

Mass spectrometry and isotope tracing

Water-soluble metabolites were extracted with 590 µL ice-cold MeOH/H₂O (80/20, v/v) containing 0.01 µM lamivudine (Sigma-Aldrich, St. Louis, USA). After centrifugation of the resulting homogenates, supernatants were transferred to an RP18 SPE (50 mg/1 mL tubes, Phenomenex, Aschaffenburg, Germany) that had been activated with 0.5 mL CH₃CN and conditioned with 0.5 mL of MeOH/H₂O (80/20, v/v). The eluate of RP18 SPE-column was evaporated in a SpeedVac (Savant, Thermo Fisher Scientific, Waltham, USA). Dry sample extracts were redissolved in 75 µL 5 mM NH₄OAc in CH₃CN/H₂O (50/50, v/v). 15 µL supernatant was transferred to LC-vials. Metabolites were analyzed by LC-MS using the following settings: For LC-MS analysis 3 µL of each sample was applied to a XBridge Premier BEH Amide (2.5 µm particles, 100 × 2.1 mm) UPLC-column (Waters, Dublin, Ireland). Metabolites were separated with Solvent A, consisting of 5 mM NH₄OAc in CH₃CN/H₂O (40/60, v/v) and solvent B consisting of 5 mM NH₄OAc in CH₃CN/H₂O (95/5, v/v) at a flow rate of 200 µL/min at 30°C by LC using a DIONEX Ultimate 3000 UHPLC system (Thermo Fisher Scientific, Bremen, Germany). A linear gradient starting after 2 min with 100% solvent B decreasing to 10% solvent B within 23 min, followed by 16 min 10% solvent B and a linear increase to 100% solvent B in 2 min. Recalibration of the column was achieved by 7 min prerun with 100% solvent B before each injection. Ultrapure H₂O was obtained from a Millipore water purification system (Milli-Q Merck Millipore, Darmstadt, Germany). HPLC-MS solvents, LC-MS NH₄OAc, standards and reference compounds were purchased from Merck.

All MS-analyses were performed on a high-resolution Q Exactive mass spectrometer equipped with a HESI probe (Thermo Fisher Scientific, Bremen, Germany) in alternating positive- and negative full MS mode with a scan range of 69.0–1000 m/z at 70K resolution

and the following ESI source parameters: sheath gas: 30, auxiliary gas: 1, sweep gas: 0, aux gas heater temperature: 120°C, spray voltage: 3 kV, capillary temperature: 320°C, S-lens RF level: 50. XIC generation and signal quantitation was performed using TraceFinder V 3.3 (Thermo Fisher Scientific, Bremen, Germany) integrating peaks which corresponded to the calculated monoisotopic metabolite masses (MIM \pm H \pm \pm 3 mMU). Analyses were generally performed in three independent biological replicates. Notably, in contrast to reduced glutathione (GSH), intracellular oxidized glutathione (GSSG) was only detected at negligibly low concentrations.

Immunofluorescence

Cells were fixed in 4% paraformaldehyde and were permeabilized and stained for immunofluorescence as published previously.¹⁵ Anti-NRF2 (ab62352, Abcam, Cambridge, UK) or anti-ATF4 (#11815, Cell Signaling Technology, Danvers, USA) antibodies were used for immunofluorescence staining. After three PBS washing steps, secondary antibody incubation was carried out in the dark for 1 h at room temperature with Alexa Fluor 594 goat anti-rabbit IgG (11037) (Life Technologies, Carlsbad, CA, USA). Hoechst 33342 (Invitrogen, Carlsbad, CA, USA) was used for nuclear staining. Samples were analyzed by inverted fluorescence microscopy or confocal laser scanning microscopy (Leica, Wetzlar, Germany).

RNA extraction, cDNA synthesis, and RT-qPCR

RNA isolation of cell pellets was performed using TRIzol reagent (Invitrogen, Carlsbad, CA, USA) according to the manufacturer's protocol. cDNA synthesis was done using the RevertAid First Strand cDNA Synthesis Kit (Fermentas, Waltham, MA, USA) with hexamer primers in accordance with the manufacturer's protocol. RT-qPCRs were performed and analyzed with the CFX Connect Real-Time System (Bio-Rad Laboratories, Munich, Germany) using SYBR Green reagent. Gene expression was normalized to *ACTB* as housekeeping gene using the $\Delta\Delta C_t$ method. The sequences of the oligonucleotides purchased from Sigma-Aldrich (St. Louis, MO, USA) are indicated in Table S1.

Tietze assay

GSH concentrations were determined by using the modified Tietze assay.³⁹ A total of 2×10^5 cells per sample were seeded and treated as indicated. To prepare the cell pellets, they were resuspended in a mixture of 1x PBS, 5% sulfosalicylic acid (SSA; Sigma-Aldrich, St Louis, USA), and GSH assay buffer (143 mM phosphate buffer, 6.3 mM EDTA, adjusted to pH 7.5) at a ratio of 1:3. Cell solubilization was achieved by subjecting the samples to three freeze-thaw cycles followed by centrifugation (12000 rpm, 4°C, 15 min).

For the determination of glutathione (GSH) levels, assay buffer with freshly added 0.34 mM NADPH (Biomol, Hamburg, Germany), 6 mM 5-5'-dithiobis-2-nitrobenzoic acid (Sigma-Aldrich, St Louis, USA), H₂O and cell pellet supernatant were added to a 1.5 mL cuvette (in a 7:1:1:0.5 ratio). The cuvette was then incubated at room temperature for 20 min. A standard curve was generated using defined GSH concentrations ranging from 10 μ M to 320 μ M. The reaction was initiated by adding 1 U/ml of glutathione reductase (GR; Sigma-Aldrich, St Louis, USA). The concentration of GSH was determined by measuring the rate of change in absorption at 412 nm using a spectrophotometer. Duplicate measurements were taken, and the GSH concentrations were calculated by comparing them to known standard concentrations and the cell numbers.

Chromatin immunoprecipitation (ChIP)

For NRF2 chromatin immunoprecipitation in UACC-62 cells, NRF2 was stabilized with sulforaphane (7.5 μ M) for 24 h or the equivalent amount of DMSO (1:1000) before ChIP was conducted. NRF2 antibody (ab62352, Abcam, Cambridge, UK) was used for immunoprecipitation.^{15,59} For ATF4 ChIP, 501mel cells were kept in glucose-deprived medium for 4 h to induce ATF4 expression. ATF4 ChIP sequencing was performed in human 501mel melanoma cells as described.⁶⁰ To prepare the ChIP, approximately 1×10^7 cells were harvested from 70 to 80% confluent 15 cm dishes by trypsinization. They were then collected into 50 mL Falcon tubes (Corning; Cat# 430828) and centrifuged at 800 x g for 4 min. The media was aspirated, and the cells were cross-linked by adding 45 mL of ice-cold PBS containing 0.4% paraformaldehyde. The cell suspension was rotated for 10 min at room temperature, followed by quenching with glycine to a final concentration of 0.2 M for 10 min. For lysis, the cells were resuspended in 1 mL of ChIP lysis buffer (50 mM Tris-HCl pH 8.0, 10 mM EDTA, 10 mM sodium butyrate, 1% SDS, 43PIC (Roche; Cat#05056489001)). The cell suspension was passed through a 25-gauge needle and sonicated for approximately 12 min in a Covaris S220 until obtaining 200–400 bp fragments (verified using the Agilent High Sensitivity DNA Kit on a Bioanalyzer (Agilent; Cat# 5067-4626)). The sonicated chromatin was cleared by centrifugation at 13,000 x g for 10 min, and the supernatant was diluted 8-fold in ChIP dilution buffer (16.7 mM Tris pH 8.0, 167 mM NaCl, 1.2 mM EDTA, 1% Triton X-100, 0.01% SDS). Sonicated chromatin was incubated with NRF2 antibody ([EP1808Y], ab62532, abcam, Cambridge, UK) or rabbit polyclonal anti-ATF4 antibody (#11815, Cell Signaling Technology, Danvers, USA), respectively, and was rotated overnight in a 50 mL Falcon tube.

For immunoprecipitation, Dynabeads G were washed, resuspended in ChIP dilution buffer, and blocked overnight with 0.5 mg/mL BSA. Immunoprecipitation was performed using the blocked Dynabeads, which were rotated for 1 h at 4°C. The beads were washed three times with low salt wash buffer (20 mM Tris-HCl pH 8.0, 150 mM NaCl, 2 mM EDTA, 1% Triton X-100, 0.1% SDS), high salt wash buffer (20 mM Tris-HCl pH 8.0, 500 mM NaCl, 2 mM EDTA, 1% Triton X-100, 0.1% SDS), and LiCl wash buffer (10 mM Tris-HCl pH 8.0, 250 mM LiCl, 1 mM EDTA, 1% sodium deoxycholate, 1% NP-40), with each wash transferred to a new DNA LoBind tube

(Eppendorf; Cat# Z666548). The beads were then eluted in 0.2 mL elution buffer (100 mM NaHCO₃, 1% SDS). To reverse cross-linking of the ChIPed DNA, the eluted material was incubated overnight at 55°C with the addition of 0.3 M NaCl (final concentration), 20 mg RNase A (Invitrogen; Cat# 12091021), and 20 mg Proteinase K (Roche; Cat# 311582800). ChIPed DNA was recovered using a QIAquick PCR Purification Kit (Qiagen; Cat# 28106). Purified ChIP-DNA was quantified using the Qubit DNA quantification assay system (Thermo Scientific, Waltham, USA). Precipitated DNA was amplified with specific primers encompassing enriched NRF2 binding peaks by real-time PCR. The oligonucleotides are displayed in [Table S1](#). For ChIP sequencing, 4 ng DNA were used for cDNA libraries preparation using the NEBNext Ultra II DNA Library Prep Kit for Illumina (New England Biolabs, Ipswich, USA) according to the manufacturer's instructions. DNA fragments were amplified by 12 cycles of PCR and library quality was analyzed with a Fragment Analyzer (Agilent, Santa Clara, USA). Sequencing was done using a NextSeq500 or HiSeq4000 Illumina platform (San Diego, USA).

QUANTIFICATION AND STATISTICAL ANALYSIS

Generally, the graphs show the arithmetic mean values of at least 3 datapoints, unless indicated otherwise, with error bars representing standard deviations. Individual values, representing independent biological samples, are shown in each graph. Data were analyzed using GraphPad Prism software, with the statistical tests described in the figure legends. p values correlate with symbols as follows, ns = not significant, *p < 0.05; **p < 0.01; ***p < 0.001.